PREDICTION OF ROCKBURST AT

MUFULIRA MINE, COPPERBELT, ZAMBIA

Dissertation for the Degree of Doctor of Engineering

Pardon SINKALA

Laboratory of Global Resources and Environmental Systems

Division of Sustainable Resources Engineering

Graduate School of Engineering

Hokkaido University

March 2023

Acknowledgements

Abstract

The overall aim of this study is to provide methods for prediction of rockburst in deep underground mines, using Mufulira mine in Zambia's Copperbelt as a case study. For over 40 years, Mufulira underground copper mine has been recording incidents of rockburst. Laboratory tests and numerical analyses were carried out to understand the rockburst mechanism at the Mufulira mine. Rockburst did not occur in the chain pillars or at the mining face, but mainly in the mining drives along diminishing pillars or ahead of the mining face. RQD suggested that the rock mass in the rockburst areas was relatively intact. Laboratory tests confirmed that the rock at Mufulira mine is very strong and brittle. Elastic stress analyses for the rockburst sites by 3-D Displacement Discontinuity Method (DDM) indicated very high stress in the chain pillars and low-stress concentration at the sites of rockburst during the initial mining stages. However, there was no apparent positive correlation between the elastically calculated normal stress values and the occurrences of rockbursts. The 2-D elastic FEM analysis was conducted under the concentrated stress by DDM and indicated some stress increase with face advance for the rockburst in the vicinity of the mining face. However, stress severity indicated almost no increase, and the rockbursts cannot be explained as an instantaneous rock mass failure due to stress increase by mining. Therefore, a creep damage model was proposed to clarify the mechanism of the rockbursts. Cumulative rock damage was evaluated for the edge elements of each sidewall of the mining drives, based on the normal stresses by 3-D DDM. The rockburst occurrences were well hindcasted. Elastoplastic analysis could not successfully predict the M2.8 rockburst. A method to estimate the volume of the rockburst source was proposed, and a likely result was obtained.

Contents Page No.

1. Introduction

1.1 A brief overview on rockburst

For over 40 years, Mufulira underground copper mine in the Copperbelt in Zambia has been recording incidents of rockburst. In January 2018, the mine recorded a rockburst at 1440 mL underground with a magnitude of 2.8. Rockburst is undesirable in the underground working environment, possibly leading to injuries or death of the workers, production loss, and equipment damage. Therefore, the authors conducted a study on the M2.8 rockburst based on field investigation, rock testing, and numerical elastic stress analysis (Sinkala et al., 2019). They further investigated other rockbursts events and re-examined the M2.8 rockburst (Sinkala et al., 2022).

Rock failure occurs everywhere. Microseismic events occur under triaxial stress far from the excavation. However, rockbursts occur almost under uniaxial or biaxial stress near or at the excavation surface. Fig 1.1 shows a typical rockburst case that occurred at Kolar Gold Fields with intense damage of steel set supports.

Fig. 1.1 Intensely damaged steel set supported drives at Kolar Gold Fields. [Photogragh from Fairhurst (1988) and Caw (1956)].

1.1.1 *Definition of rockburst*

Different authors have defined rockburst in various ways. Rockburst is a sudden or violent damage in an excavation associated with microseismicity (Hedley, 1992; Kaiser et al., 1996; Kaiser and Cai, 2012). Sheng-Jun et al. (2016) defined a rockburst as a brittle failure that occurs suddenly and is induced by high stress. Tian-Hui et al. (2018) suggested that rockburst is sudden rock mass failure that occurs with sudden strain energy release, and they also discussed several other definitions from different authors. However, in this research, rockburst can be defined as a violent rock mass failure, emitting loud acoustic sound, and often with violent expulsion of rock fragments from an underground excavation. Based on this definition, the main aspect of rockburst can be obtained: violent failure, loud acoustic sound, and violent expulsion of fragments.

1.1.2 *Types and mechanisms of rockburst*

There are many contributions from different researchers that explain various types of rockburst and their mechanisms. Muller (1991) and He et al. (2012) explained different rockburst types classified as strain burst, fault-slip burst, and pillar burst. A strain burst relieves the stored strain energy in a high-stress zone of the rock mass surrounding an excavation. Malovinchko (2020) described strain burst as a sudden violent failure of rock near an excavation boundary caused by excessive straining of an un-fractured volume of rock. According to Ortlepp and Stacey (1994), strain bursting is more likely to occur in more massive rock types than in significantly jointed and fractured rock masses. When shear failure occurs along the surface of a major discontinuity, it can be regarded as a fault-slip burst. A pillar burst is a rockburst that occurs in an underground pillar due to stress conditions and pillar dimensions. The rockburst mechanism can be related to strain relaxation of the rock mass surrounding newly mined areas and the dynamic response of the rock to blast-induced waves (Ben-Guo et al., 2016). Kaiser and Cai (2012) defined rockburst damage in three categories; (1) bulking as a result of fracturing, (2) expulsion of rock from the surface due to transfer of seismic energy, and (3) rockfall, which is induced by microseismic vibration. He et al. (2018) stated that a rockburst might occur in the following two conditions: (1) failure of highly stressed rock masses that store a large amount of strain energy during tunnel excavation or face stoping, and (2) failure in less stressed and deformed rocks that store less strain energy after excavation. The failure is induced by external disturbances such as blasting, caving, and tunneling in adjacent areas. In our cases, the rockbursts cannot be classified in any of the two categories. Stress concentration is in between the two cases and rockbursts are induced by time-dependent rock deformation as brittle creep failure.

1.1.3 *Indexes of rockburst potential*

There have been several indexes proposed to represent rockburst potential (He et al., 2021; Askaripour et al., 2022; He et al., 2022). A few of such indexes selected from literature are shown in Tables 1.1 and 1.2. The simplest index is stress value, because the conditions for rockburst occurrence include hard rock mass and high stress (ex. Jaeger and Cook, 1979). Sepehri et al. (2020) carried out a state-of-the-art full 3-D stress analysis using finite element method (FEM) for a diamond mine. They calculated tangential stress at the rock surface and used it to represent rockburst potential. Energy release rate would be the most famous index. The index can be obtained from elastic theory as strain energy release due to mining from the entire elastic medium containing the mining panel divided by the face advance (Jaeger and Cook, 1979). Fujii et al. (1997) proposed strain energy release rate from fracturing rock mass divided by the face advance. Sainoki et al. (2016) analyzed fault behavior for seismicity in a Canadian metal mine.

Numerical stress analysis is required to obtain such indexes. Several continuum- and discontinuum-based numerical methods have been applied to solve problems of rock failure in the past decades. Each of these methods has disadvantages, and none of the methods has absolute advantages over other methods. The selection of an appropriate method, therefore, depends on problem-specific factors (Jing, 2003). The most popular stress analysis method is FEM. However, mine-wide 3D stress analysis manipulating hundreds of mining steps by FEM would take time. Instead, 3D elastic stress analyses using the Displacement Discontinuity Method (DDM) (Crouch and Fairhurst, 1973; Crouch, 1976) were carried out to show changes in stress levels around the rockburst sites in Sinkala et al. (2019). DDM is a kind of Boundary Element Method (BEM) developed particularly for problems associated with tabular mining. The BEM obtains solutions using only boundary data while automatically satisfying governing equations in the interior region (Mack and Crouch, 1988). The above feature gives BEM an advantage to solve large-scale problems, with minimum computer memory requirement compared to other numerical methods. DDM is also efficient and economical and can quickly estimate displacements and stresses around underground excavations due to mining (Crouch, 1976), approximating the ore body, mined-out areas, and roadways by crack-like displacement discontinuity elements with and without thin inclusions. Using the displacement discontinuity elements makes DDM suitable for the analysis of stress disturbances by tabular mining such as coal mining. At Mufulira mine, the orebody is relatively thicker than usual cases in tabular mining. However, DDM can still be applied to roughly but also rapidly estimate the changes in stress distribution with progress in mining at a larger scale.

Sinkala et al. (2019) calculated the normal stress to the orebody at the M2.8 rockburst and its variation with face advance by the 3-D DDM. However, the elastically predicted stress at the rockburst site was not very high and barely increased with the face advance. This study applies DDM with a larger model to investigate other rockburst events from 2016 to 2018 and re-examine the M2.8 rockburst. Again, it will be shown that normal stress value or its increase with face advance cannot explain rockburst occurrences. Therefore, more precise stress analysis by a 2-D finite element method (FEM) on the rockburst sections is also carried out under the boundary conditions based on the mine-wide 3-D DDM results. However, it will be shown that stress severity cannot explain the rockburst occurrences. Finally, the creep damage model is proposed under an assumption that the rockbursts could be brittle creep failure of the relatively intact rock mass, and it well hindcasts the rockbursts occurrences.

Table 1.1 Stress indexes of rockburst.

Index	Equation	Rockburst risk				Description
		None	Low	Medium	High	
Stress index (S_i) (Yoon, 1994)	$S_i = \dfrac{\sigma_c}{\sigma_v}$	-	-	$2.5 \leq S_i \leq 5$	$S_i \leq 2.5$	σ_c is the UCS of rock and σ_v is the vertical component of in situ stress.
Tangential stress (T_s) (Wang et al., 1998; Hoek & Brown, 1980)	$T_s = \dfrac{\sigma_\theta}{\sigma_c}$	$T_s < 0.3$	$0.3 \leq T_s < 0.5$	$0.5 \leq T_s < 0.7$	$T_s \geq 0.7$	σ_θ is tangential stress around an excavation opening and σ_c is the UCS of rock.
Turchaninov method (T_m) (Turchaninov & Markov, 1981; He et al., 2021)	$T_m = \dfrac{\sigma_\theta + \sigma_n}{\sigma_c}$	$T_m < 0.2$	$0.2 \leq T_m < 0.4$	$0.4 \leq T_m < 0.5$	$T_m \geq 0.5$	σ_θ is tangential stress, σ_n is normal stress and σ_c is the UCS of rock.
Barton method (B_m) (Barton et al., 1974)	$B_m = \dfrac{\sigma_1}{\sigma_c}$	$B_m < 0.15$	$0.15 \leq B_m < 0.2$	$0.2 \leq B_m < 0.4$	$B_m \geq 0.4$	σ_1 is the maximum principal stress and σ_c is the UCS of rock.
Modified Russenes method (R_m) (Russenes, 1974; He et al., 2021)	$R_m = \dfrac{\sigma_{\theta max}}{\sigma_c}$	$R_m < 0.2$	$0.2 \leq R_m < 0.3$	$0.3 \leq R_m < 0.4$	$R_m \geq 0.4$	$\sigma_{\theta max}$ is the maximum tangential stress and σ_c is the UCS of rock.
Brittleness coefficient method (BC) (Wang & Park, 2001; Wang et al., 2018)	$BC = \dfrac{\sigma_{sc}}{\sigma_t}$	$BC \geq 40$	$26.7 \leq BC < 40$	$14.5 \leq BC < 26.7$	$BC < 14.5$	σ_{sc} is the uniaxial saturated compressive strength and σ_t is the uniaxial tensile strength of rock.
Brittle deformation coefficient method (K_u) (Neyman et al., 1972)	$K_u = \dfrac{\sigma_t}{\sigma_1}$	$K_u \leq 2$	$2 < K_u \leq 6$	$6 < K_u \leq 9$	$K_u > 9$	σ_t is the tensile strength of rock and σ_1 is the maximum principal stress.
Tao discriminant index (α) (Tao, 1988)	$\alpha = \dfrac{\sigma_c}{\sigma_1}$	$\alpha > 14.5$	$5.5 < \alpha \leq 14.5$	$2.5 < \alpha \leq 5.5$	$\alpha \leq 2.5$	σ_c is the UCS of rock and σ_1 is the maximum principal stress.

Table 1.2 Energy indexes of rockburst.

Index	Equation	Rockburst risk				Description
		None	Low	Medium	High	
Linear elastic energy (W_{et}) (Wang & Park, 2001)	$W_{et} = \dfrac{\sigma_c^2}{2E_u}$ (KJ/m^3)	$W_{et} < 50$	$50 < W_{et} < 100$	$100 \le W_{et} < 200$	$W_{et} > 200$	σ_c is the UCS of intact rock and E_u is the elastic modulus.
Elastic strain energy (EN_i) (Sirait et al., 2013; Kidybin´ski, 1981)	$EN_i = \dfrac{EN_e}{EN_p}$	$EN_i < 2$	$2 \le EN_i < 5$	-	$EN_i \ge 5$	EN_e is the elastic strain energy saved before failure, and EN_p is the plastic strain energy consumed after failure.
Brittleness index modified (BIM) (Aubertin et al., 1994)	$BIM = \dfrac{\phi_t}{\phi_e}$	-	$BIM > 1.5$	$1.2 < BIM < 1.5$	$1.0 < BIM < 1.2$	ϕ_t is the total input energy at peak and ϕ_e is the peak elastic strain energy obtained during UCS test.
Burst efficiency ratio (η) (Kidybin´ski, 1981; Singh, 1989)	$\eta = \dfrac{\phi_k}{\phi_0} \times 100$	$\eta < 3.5\%$	$3.5\% \le \eta < 4.2\%$	$4.2\% \le \eta < 4.7\%$	$\eta \ge 4.7\%$	ϕ_k is the throw energy of chips and ϕ_0 is the maximum elastic strain energy obtained by UCS test.
Energetic rockburst indicator (T_e) (Tajdus´ et al., 1997)	$T_e = \dfrac{E_k}{E_k^0}$	$T_e < 1$	$T_e \ge 1$			E_k is the kinetic energy of the crushed rock mass discharged to an opening and E_k^0 is the minimum kinetic energy required to initiate rockburst.
Excess shear stress (τ_e) (Ryder, 1987)	$\tau_e = \left\lvert \tau \right\rvert - \tau_d$ $= \left\lvert \tau \right\rvert - \mu\sigma_n$ $= \left\lvert \tau \right\rvert - (\tan\phi)\sigma_n$	$\tau_e < 5$ MPa	$\tau_e \ge 5$ MPa for a plane of weakness $\tau_e \ge 20$ MPa for intact rock			τ is the shear stress before slip and τ_d is the dynamic strength of plane, μ is the coefficient of friction, ϕ is the angle of dynamic friction and is approximated as 30° under dynamic conditions.

1.1.4 *Rockburst monitoring*

Currently there are several methods of monitoring and identifying potential rockburst-prone zones. Research and industrial practice on the estimation and identification of rockburst-prone zones mainly focuses on theoretical analysis, numerical simulation and field measurement, as proposed by Fei et al. (2018). Field measurement includes the use of a microseismic monitoring system.

1.2 Objectives

The main objectives of this research are;

1. To propose a model that can predict rockburst occurrences.

2. To investigate the following prevention methods for rockburst, using the above;

   i. Change in mining sequence.

   ii. Change in mine geometry, by partial or full elimination of pillars.

1.3 Content of the research

In chapter 2, explanation of the background of Mufulira Mine is given. An explanation about the mine geology and the mining method is presented. The microseismic monitoring system, as well as its objectives is explained. Statistical data of seismic events and the rockbursts is provided. Findings from geological and geotechnical field investigations conducted at Mufulira mine are discussed. RQD measurements also suggest that the rock mass near rockburst sites was relatively intact.

In chapter 3, results from laboratory experiments are discussed. These experiments include Brazilian test, uniaxial compression and triaxial compression tests. Results of the experiments justify that the rock at Mufulira mine is extremely strong and brittle.

In chapter 4, the mine-wide distribution of induced stresses with face advance in ore extraction is provided, based on 3D DDM. Stress analysis showed very high stresses in the chain pillars and low stress concentration at the rockburst site during initial stages of mining. But later, stress levels gradually increased with mining. More accurate distribution of stresses at rockburst faces by 2D FEM is given. Based on the 2D FEM, the modified stress severity indicated almost no increase, implying that the rockbursts cannot be explained as an instantaneous rock mass failure due to stress increase by mining.

In chapter 5, the creep damage model is proposed and explained. Results of cumulative rock damage of edge elements of each sidewall of the mining drives are provided. The rockburst occurrences were well hindcasted by the model. Results showing the effect of changing the mining sequence and pillar elimination on potential rockbursting are also provided.

In chapter 6, an original elasto-plastic analysis method is proposed and explained. This is an attempt to prevent shortcomings observed in creep analysis so far. Results of normal stress distribution and element failure are presented. So far, elasto-plastic analysis cannot predict the rockburts successfully.

In chapter 7, a method to estimate the volume of the rockburst source is also proposed, and the likely results are obtained.

In chapter 8, the conclusions and recommendations are made, and suggestions for future work are provided.

2. Background of Mufulira

2.1 Geology

Mufulira mine hosts sulfide orebodies comprising the Neoproterozoic meta-sedimentary rocks belonging to the Katanga Supergroup. The mine has three orebodies; A, B, and C (Fig. 2.1), which consist mainly of quartzite and occur in the form of mineralized bands, which are bedded or of stratiform type (Brandit, 1962). Thin sectional images of rock samples are shown in Fig. 2.2. The C orebody quartzite indicated (arkosic) sandstone severely disturbed, coarse-grained, and poorly sorted, with bornite, chalcopyrite, and chalcocite as ore-forming minerals. The footwall quartzite indicated poorly sorted, granular to grained (arkosic) sandstone features. The observed minerals in footwall quartzite consist of orthoclase, granite, spinel, plagioclase, and quartz. Secondary minerals were identified as anhydrite and sericite in footwall quartzite and orebody quartzite.
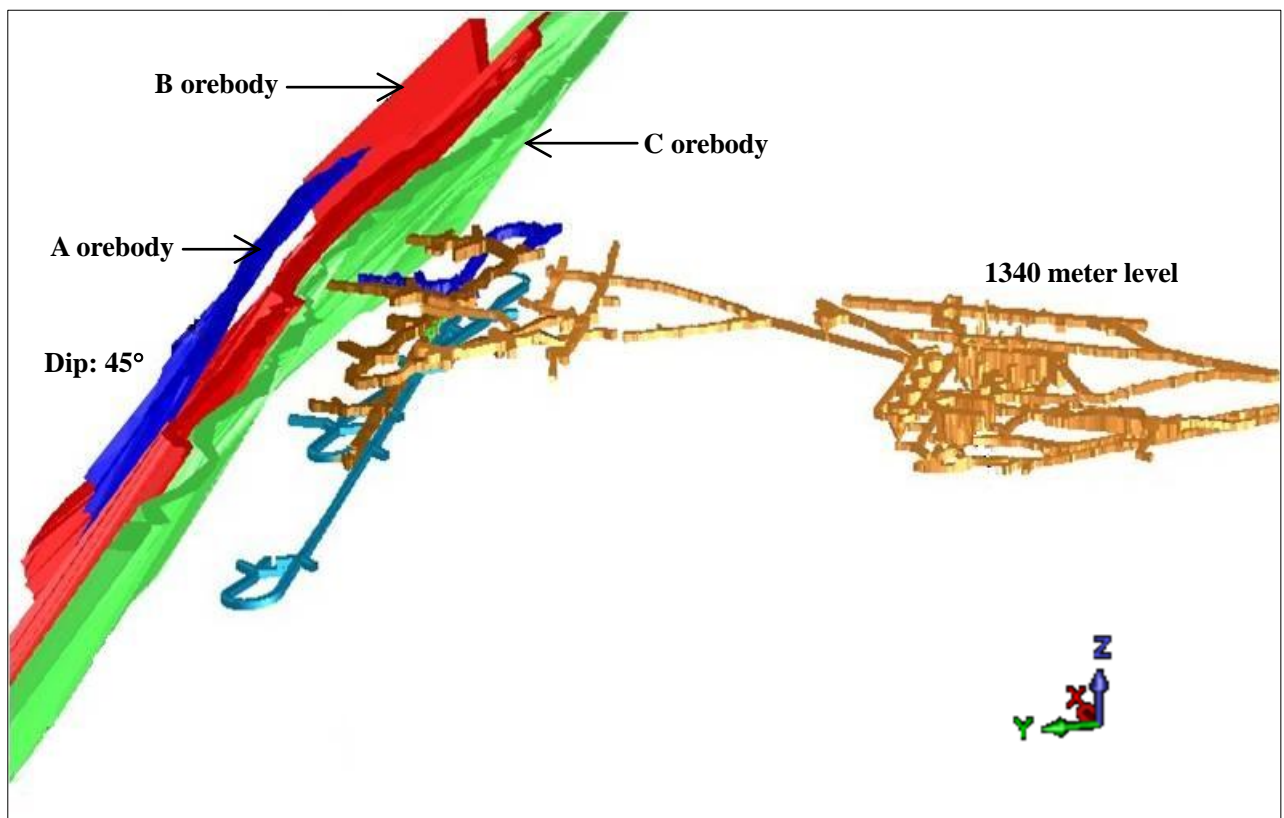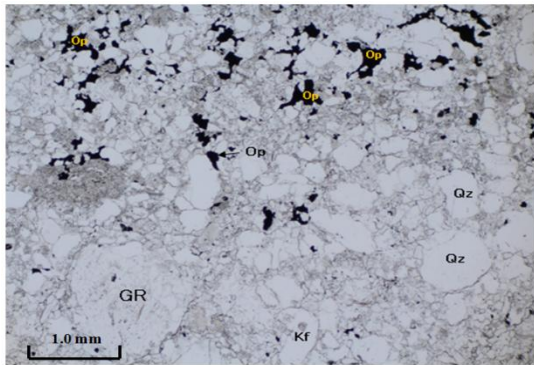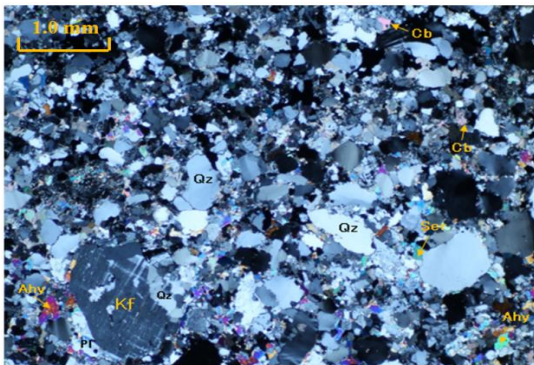

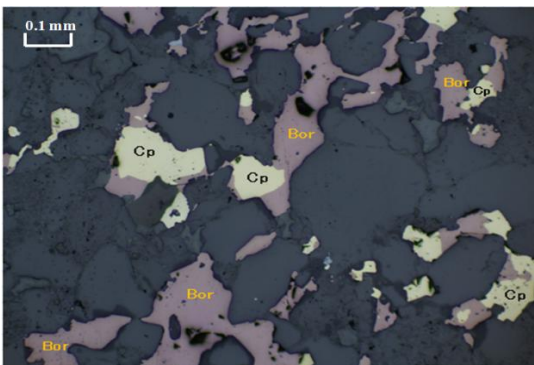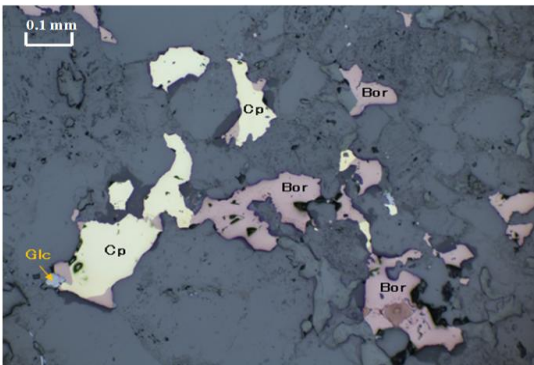Fig. 2.1 The underground structure of Mufulira mine.

C orebody quartzite

Footwall quartzite

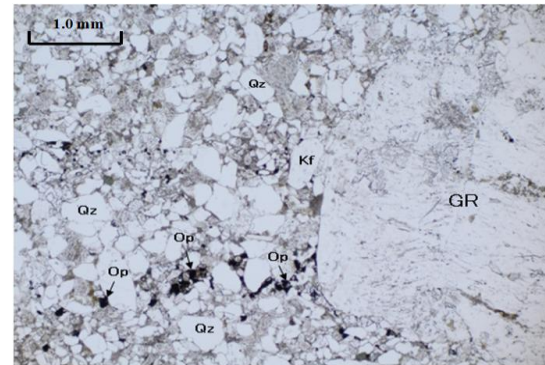(a) Low magnification, Open Nicol

(e) Low magnification, Open Nicol

(b) Low magnification, Crossed Nicols

(f) Low magnification, Crossed Nicols

(c) High magnification, Open Nicol

(g) High magnification, Open Nicol

(d) High magnification, Crossed Nicols
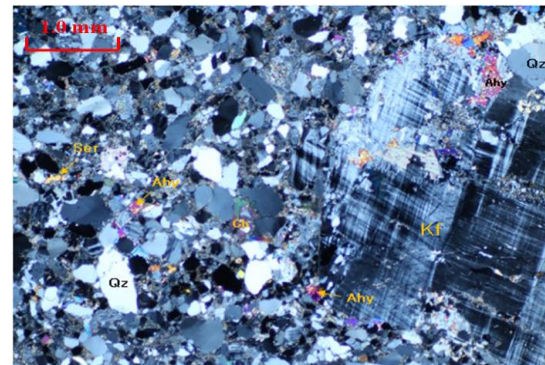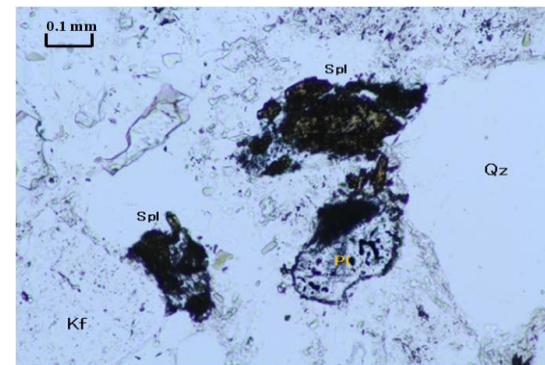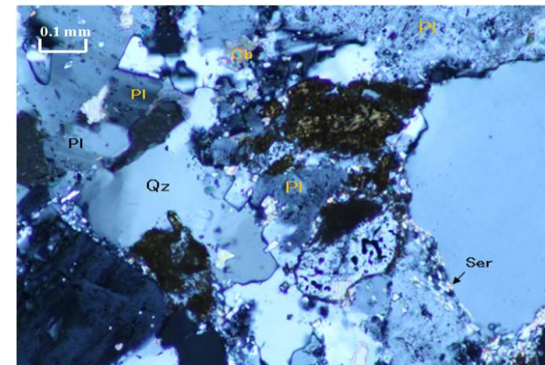
(h) High magnification, Crossed Nicols

Fig. 2.2 Microscope images of Orebody Quartzite in C-orebody (a, b, c, d) and Footwall Quartzite (e, f, g, h). [QZ: Quartz, Kf: Orthoclase, Pl: Plagioclase, Ser: Sericite, Bor: Bornite, Cp: Chalcopyrite, Spl: Spinel, Clc: Chalcocite, Ahy: Anhydrite, Cb: Carbonate mineral, Op: Opaque mineral, GR: Granite fragments].

11

The orebodies dip at an average of 45° towards the northeast, covering approximately 7 km in strike length, divided into mining blocks of 100 m each in length (Fig. 2.3).
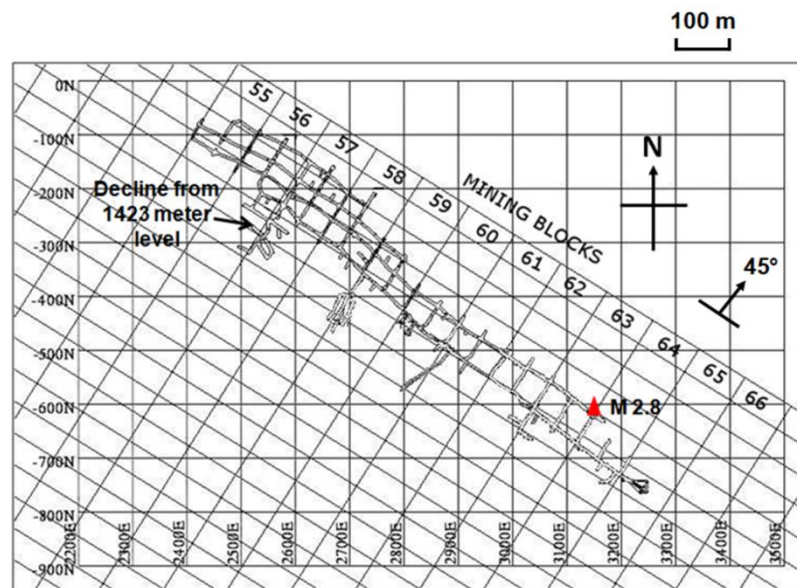

Fig. 2.3 Typical underground mine layout at Mufulira mine (at 1440 mL, indicating M 2.8 rockburst).

2.2 Mine layout and methods

As shown in that Fig. 2.3, a typical layout of a mining level at Mufulira mine consists of access crosscuts linked to the decline system and driven towards the orebody on various levels. Roadways referred to as footwall drives are then mined in the footwall along its strike at the end of these access crosscuts. Multiple orebody crosscuts lead into mining drives driven in the orebody along its strike from the footwall drive. The mining drives, footwall drives, and crosscuts are 4 m wide and 4 m high. Orebody crosscuts may be further driven through the orebodies from the mining drives at intervals determined by the selected mining method.

The mine applies the Mechanized Continuous Retreat (MCR) mining method, a variation of sublevel open stoping. One, two, or three sublevels are drilled in each MCR 1, 2, or 3 categories. Fig. 2.4 shows a typical layout of MCR 2. The method consists of fan long holes drilled in the roof of a mining drive, leaving a small pillar known as a chain pillar. The chain pillar helps prevent the broken material of the hanging wall from the upper levels from diluting the blasted ore (Ng'ambi and Mutambo, 2016). The sublevels are at 17 m spacing intervals. The mining level serves for stope drilling only. After blasting, the ore is collected from the drawing level.
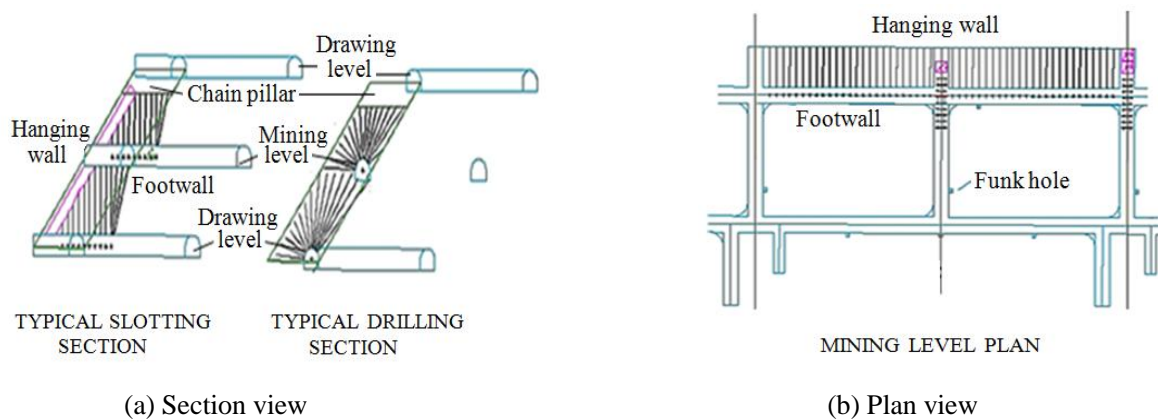
(a) Section view   (b) Plan view

Fig. 2.4 Typical Mechanized Continuous Retreat Mining method at Mufulira mine (MCR 2).

2.3 Mine seismicity

2.3.1 Seismic monitoring system

In an effort to reduce rockburst risk, Mufulira mine has installed a microseismic monitoring system. Seismic monitoring at the mine enables for quantitative observations of the levels of seismicity at any given time. The primary purpose of this system is to record microseismicity, and the data obtained is then used to identify potential unstable areas within the mine. These unstable areas are either supported or reinforced to mitigate the risk of damage. Therefore, it is a tool that guides efforts towards warning, monitoring and control of potential rockmass instabilities that could result in rockbursts. The following below are some of the objectives of the seismic monitoring system;

(a) Location of potential rockbursts;

One of the key objectives is to provide management with locations and magnitude of seismic events. Locations of intermediate or large seismic events may be regarded as potential rockburst areas. Such information would assist management to introduce and carry out possible measures to manage potential rockburst.

(b) Warnings;

Unexpected strong changes in the spatial behavior of seismic parameters or any identification of certain defined characteristic patterns may have significant effects of leading to dynamic instabilities in the underground mine. Similarly, this would enable management to facilitate for measures to manage potential rockbursts.

(c) Monitoring;

Over time, management may be able to detect spatial-temporal changes in seismic parameters, for instance an increase in the number of intermediate and large size events and in their time distribution, and variations in seismically inferred stress changes within a region of interest in the rockmass. Again, this would enable management to introduce control measures for potential rockbursts.

(d) Verification of numerical design;

To verify assumptions as well as input parameters of the numerical design process. Generally, it would be very important to confirm some of the critical assumptions of numerical modeling, which may be reflected in improvements of seismic parameters.

(e) Back-analysis;

It is very important to carryout both seismic monitoring and numerical modeling. However, back analysis of large instabilities even if they did not result in loss of life or in considerable damage would be equally important. Back analysis of rockmass behavior associated with different mining layouts, rates of mining, or sequence of mining is an important factor for safer and more productive mining. Therefore, it is desirable to maintain the database of seismicity. Such may include times, locations, magnitudes, seismic moments, radiated energies, sizes and stress drops for all seismic events recorded. The availability of seismic parameters recorded a few months prior to large events and rockbursts, and located within a few source diameters of that event would assist in back analysis and research.

Currently, the microseismic system consists of 12 triaxial 4.5 Hz geophones with an expected coil resistance of 375 Ω for each solenoid. The geophones are installed up-hole and down-hole at approximately 12 m depth, between 500 mL and 1440 mL underground. Fig. 2.5 shows the installation units for the microseismic monitoring system at Mufulira mine, which are connected to a network structure in Fig. 2.6. As illustrated in the structure, each geophone is connected to a seismometer box by a sensor cable at a recommended distance of less than 250 m. A seismometer box contains a Net Analogue-Digital Converter, waveform processor, and data communication device. Digitized data undergoes first stage data processing by netSP (Net Signal-Processor), a waveform processor device. A communication device called the DSL (Digital Subscriber Line) Modem collects

the processed data from netSP and transmits them to the ATU (Analogue Time Unit) through the DSL Communications Cable. The timing unit generates time synchronization signals, which are sent to the seismic server via a series of fibre-optic cables and ethernet. Finally, the seismic server carries out the auto-processing of events. The server uses IMS (Institute of Mine Seismology) Synapse software.
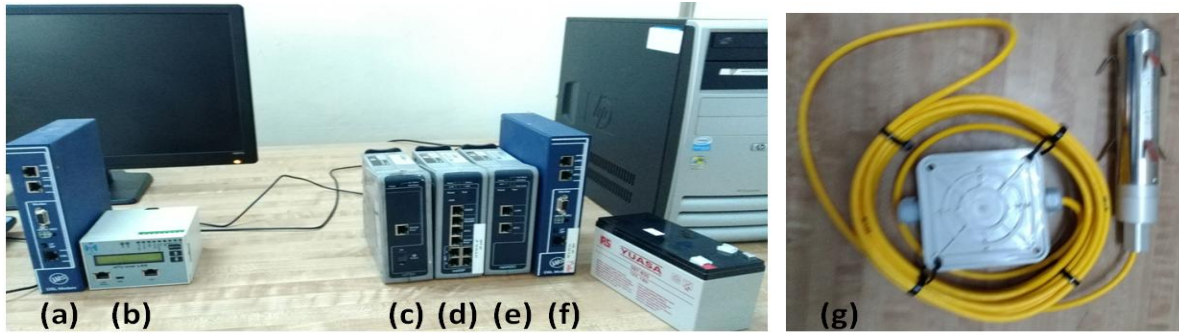

Fig. 2.5 Installation units of the seismic monitoring system [a: Digital Subscriber Line Modem (DSL), b: Analogue Time Unit (ATU), c: Uninterrupted Power Supply (UPS), d: Net Signal Processor (netSP), e: Net Analogue Digital Converter (netADC), f: Digital Subscriber Line Modem (DSL), g: Geophone] (Sinkala, 2019).
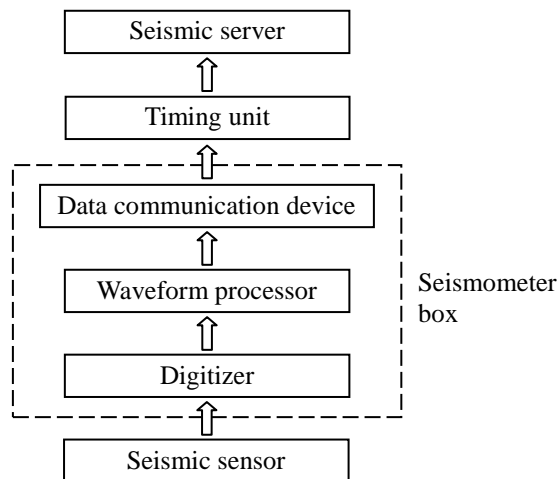

Fig. 2.6 The network structure of the microseismic monitoring system at Mufulira mine.

2.3.2 Seismic events

The microseismic system recorded one thousand microseismic events from 2016 to 2018, with a magnitude range evaluated from 0 to 3 (Fig. 2.7). And some events can be observed as rockbursts (Table 2.1).

The Gutenberg – Richter relation in Fig. 2.7a was calculated as follows;

$$\log (N) = a - bM$$

(2.1)

where N is the cumulative number, M is the magnitude, a = 3.57, and b = 1.02. Twelve events caused damage mainly around the mining drive and were regarded as rockbursts (Fig. 2.7b). The rockburst #12 (M 2.8), the largest event, closed the mining drive at 1440 m level (Fig. 2.8).

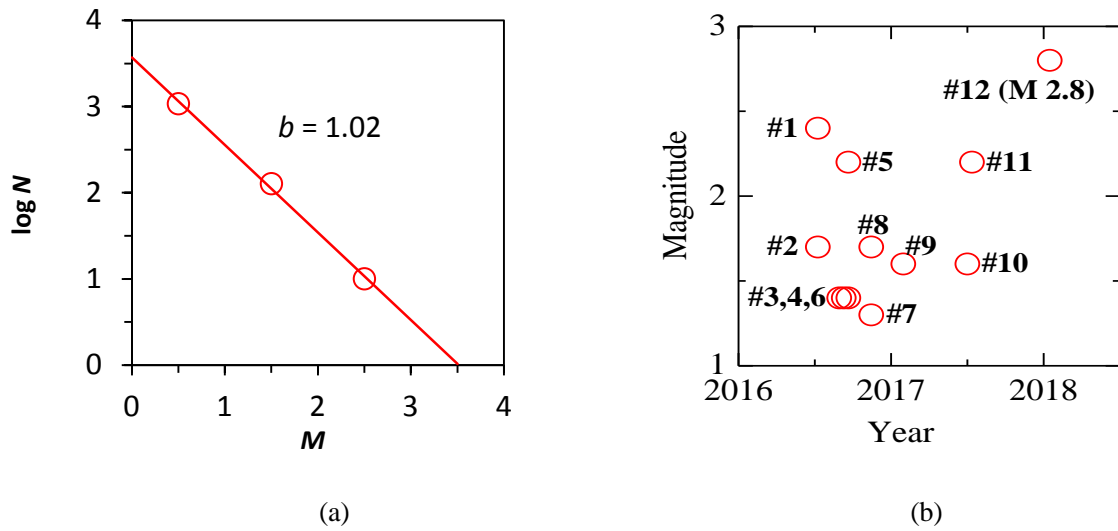(a)   (b)

Fig.2.7 Distribution of rockburst events at Mufulira underground mine from 2016 to 2018.

Fig. 2.8 Rockburst site for M2.8 (date taken: 15th March 2018).

Table 2.1 Rockburst events at Mufulira Mine from July 2016 to January 2018. Type P: Pillar burst, S: Strain burst.

Rockburst			Magnitude	Location	Type
Event	Date	Time			
#1	10th July, 2016	00:34 AM	2.4	1407 mL, block 63/64 mining drive	S
#2	10th July, 2016	01:05 AM	1.7	1407 mL, block 63/64 mining drive	S
#3	30th August, 2016	02:07 PM	1.4	1207 mL, block 53 P3 footwall drive	S
#4	10th September, 2016	04:54 PM	1.4	1423 mL, block 63/64 mining drive	P
#5	19th September, 2016	06:48 AM	2.2	1423 mL, block 63/64 mining drive	P
#6	19th September, 2016	10:53 AM	1.4	1423 mL, block 63/64 mining drive	P
#7	13th November, 2016	07:33 PM	1.3	1440 mL 62P5 Crosscut North	S
#8	14th November, 2016	07:19 PM	1.7	1423 mL block 65 east stope	S
#9	28th January 2017	03:50 AM	1.6	1440 mL block 62 east mining drive	S
#10	01st July, 2017	05:26 PM	1.6	1440 mL block 63 west mining drive	S
#11	12th July, 2017	08:43 AM	2.2	1440 mL block 56P6 west footwall drive	S
#12	16th January, 2018	05:07 PM	2.8	1440 mL block 63/64 west mining drive	P

Rockbursts #3 and #11 occurred in the footwall drives, while #7 occurred in a crosscut in the footwall (Table 2.1). The rockbursts other than #3, #7, and #11 occurred in the mining drives concentrating within a smaller orebody portion (Figs. 2.9 and 2.10). The locations in the figures are not those by the microseismic monitoring system but where the rock failure was observed. #4, #5, #6 and #12 occurred at the pillars. After #1 and #2 occurred at 1407 m level, a pillar was left during mining at 1423 m level just below the site where those rockbursts had occurred. The pillar failed many times with stress concentration leading to #4, #5, and #6 at the same location. Rockburst #6 occurred four hours later after #5. According to the definition of rockburst by He et al. (2012) and Muller (1991), the rockbursts #4, #5, #6, and #12 can be classified as pillar bursts because they occurred at pillars. The rockbursts #1, #2, #8, #9, and #10 can be classified as strain bursts because they occurred ahead of the face.
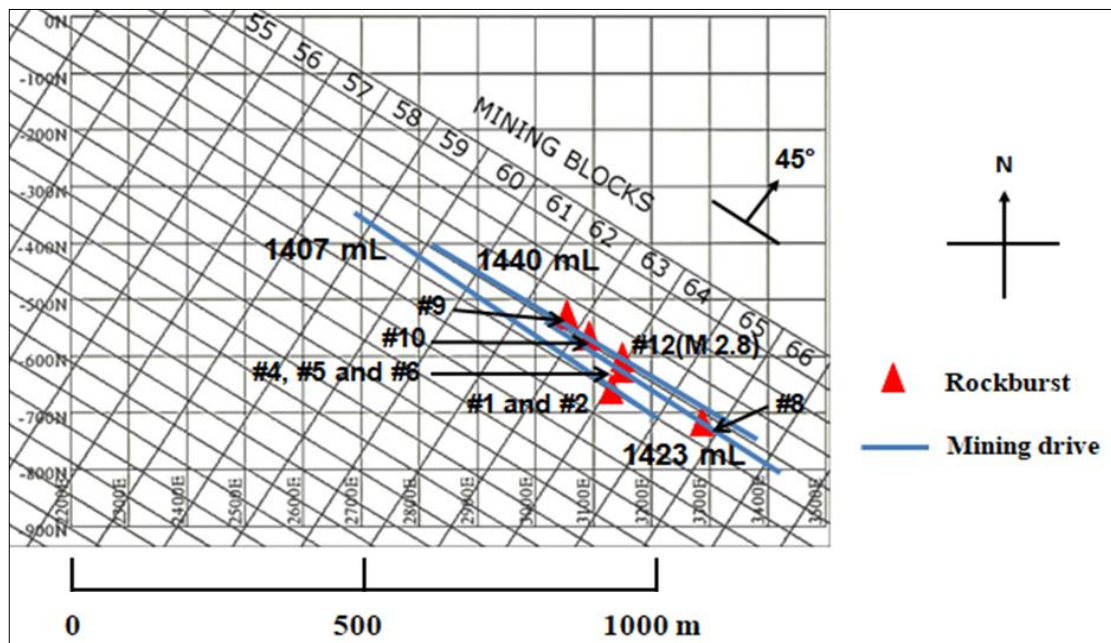
17

Fig. 2.9 Locations of rockbursts and approximate mining drive orientation (rockbursts concentrated between mining blocks 61 and 66).
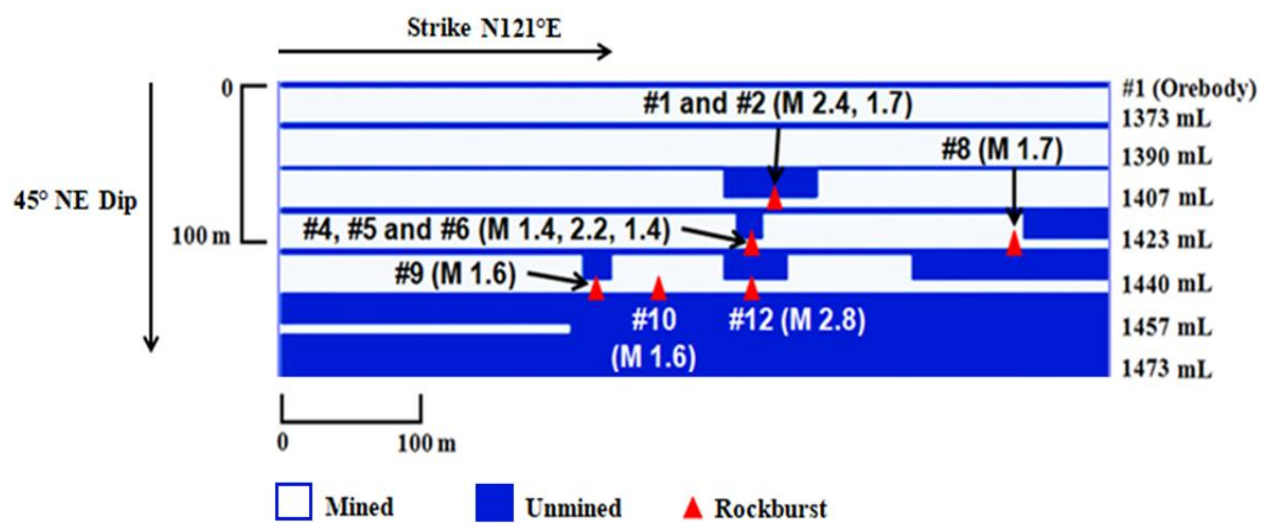

Fig. 2.10 Mine layout and rockburst sites when viewed from footwall (the mine layout is as of January 2018).

2.4 Geotechnical and geological investigation

Core logging was conducted for rock cores from boreholes (Fig. 2.11) drilled horizontally towards the hanging wall at1423 and 1457 m levels. From the core logging data, Rock Quality Designation (RQD) was calculated using Eq. (2.2). And the results for each core, showing the variation of RQD with horizontal depth are represented in Fig. 2.12.

$$RQD\ (\%) = 100 \sum_{i=1}^{n} \frac{x_i}{L} \tag{2.2}$$

where x_i represent core pieces greater than 0.1m, and L is total core length.


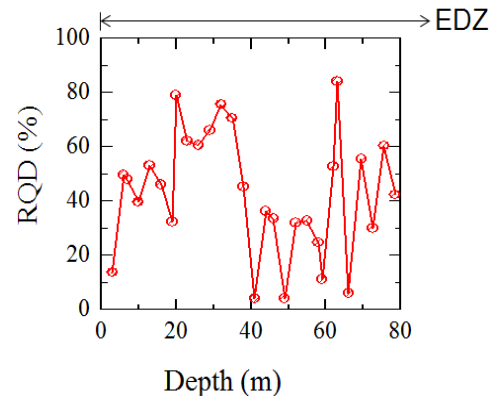(a) Tray of drilled core from 1423 meter level.   (b) Mufulira Mine core shed.

Fig. 2.11 Borehole cores at Mufulira Mine

Excavation Damaged Zone, EDZ (Perras and Diederichs, 2016) at 1457 m level (Fig. 2.12a) was approximately 10 m because the rock mass was nearly virgin. On the other hand, it extended to greater than 80 m at 1423 M Level (Fig. 2.12b) because of mining disturbance. The rock mass conditions at 1440 meter level were assumed to be intermediate between 1423 meter level and 1457 meter level. Therefore an average RQD value of 64.5% between the two levels was calculated, and this value was assumed to be the RQD for 1440 meter level.
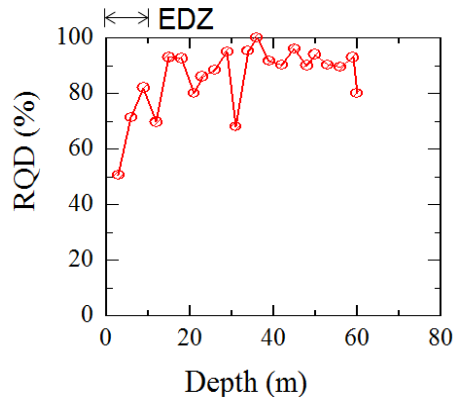
(a) At 1457 meter level   (b) At 1423 meter level

Fig. 2.12 Variation of RQD with horizontal depth.

Later, RQD was used to calculate the modulus of elasticity of the rock mass using the modulus of elasticity of a sample specimen. Zhang and Einstein (2004) explained this method as provided in Fig. 2.13 and Eq. (2.3). Results obtained from the calculation of RQD and modulus of elasticity are provided in Table 2.2.
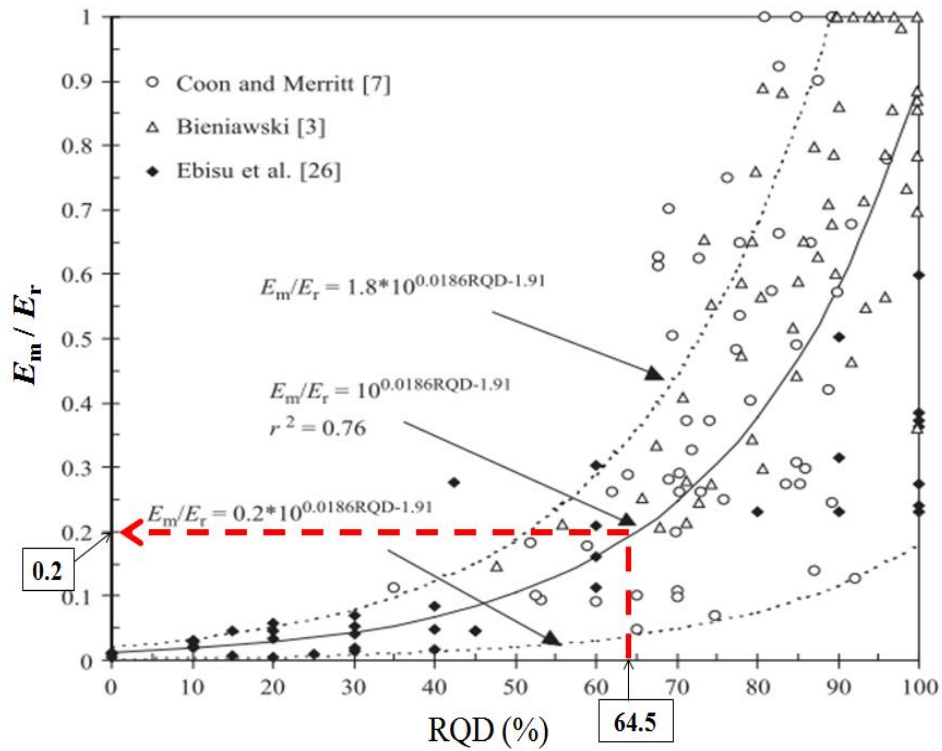

Fig. 2.13 Estimation of deformation modulus of rock mass using the deformation modulus of a rock specimen (Zhang and Einstein, 2004).

$$\frac{E_\mathrm{m}}{E_\mathrm{r}} = 10^{0.0186\,RQD - 1.91} \qquad (2.3)$$

Where E_m is tangent modulus of rock mass, and E_r is tangent modulus of rock specimen. In this study, E_m was estimated based on the corrected tangent modulus of rock specimen (E_50r).

Table 2.2 Estimated RQD and tangent modulus ratio.

Average RQD	$E_\mathrm{m}/E_\mathrm{r}$	E_r (GPa)	E_m (GPa)
64.5	0.2	69.5	13.9

3. Rock testing

3.1 Sample preparation

In order to understand rock properties at Mufulira Mine, rock specimens were prepared for experiments. The process began with rock drilling as shown in Fig 3.1 (a). The remaining process involved rock cutting and grinding to make cylindrical core specimens, prepared from both footwall quartzite and orebody quartzite, having approximate dimensions of diameter 30 mm and length 60 mm for one set. Another set of specimens was also prepared having approximate dimensions of diameter 30 mm and length 30 mm. Two weeks before starting rock experiments, the samples were kept in containers as shown in Fig 3.1 (b). These containers were then sealed, keeping 100% relative humidity and a temperature of 295K as shown in Fig 3.1 (c). This was done in order to keep the specimens in consistency with in-situ conditions of the rock mass.

(a) Rock drilling process (at Hokkaido University Rock Mechanics Laboratory).

(b) Inside the container.

(c) Sealed container with 100% humidity.

Fig 3.1 Preparation for rock specimens.

3.2 Brazilian test

3.2.1. Methods

After keeping specimens in sealed containers at 100% relative humidity and a temperature of 295K for two weeks, Brazilian disk test using an Instron 5500R loading frame (Fig 3.2) was carried out on the specimens. The specimens had approximate dimensions of diameter 30 mm and length 30 mm. The indirect tensile strength was calculated using the following expression below.

$$T_0 = \frac{2F_{\max}}{\pi \cdot d \cdot l} \qquad\qquad (3.1)$$

where $F_{\max}$ (N) is the maximum compressive load, d (m) is specimen diameter, and l (m) is specimen length.

Fig 3.2 Instron loading frame used in the experiment.

3.2.2 Results

Observations on behavior of specimens on loading mainly indicated fracture planes cutting the bases of the cylindrical specimens through the central axes. Fig 3.3 shows the behavior of specimens on loading for both orebody quartzite and footwall quartzite.

Fig 3.3 Fractured specimens after Brazilian test.

The results of the indirect tensile strength are shown in Tables 3.1 and 3.2. And, Fig 3.4 and 3.5 show stress-stroke graphs for both footwall quartzite and orebody quartzite test samples.

Table 3.1 Indirect Tensile Strength of footwall quartzite.

FWQ Sample No.	Weight (g)	Density (kg/m^3)	Indirect Tensile Strength (MPa)
17	53.6	2528	13.04
18	53.0	2499	11.43
19	54.2	2556	19.07
22	55.4	2612	16.25
24	53.3	2513	12.23
Average	53.9 ± 0.949	2542 ± 44.7	14.40 ± 3.19

Table 3.2 Indirect Tensile Strength of orebody quartzite.

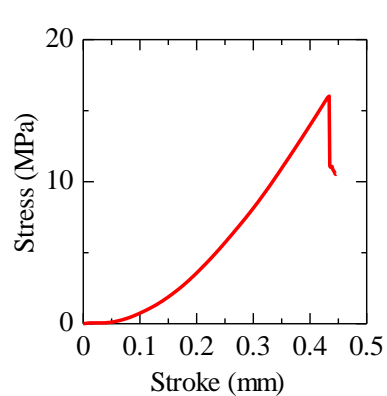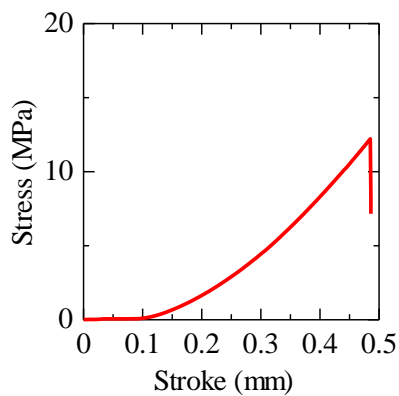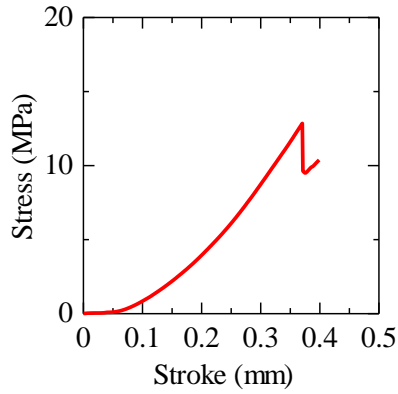| OBQ Sample No.	Weight (g)	Density (kg/m^3)	Indirect Tensile Strength (MPa)
14	56.9	2683	13.03
15	58.5	2759	15.45
18	57.1	2693	12.77
19	56.8	2679	14.38
Average	57.3 ± 0.793	2703 ± 37.4	13.91 ± 1.25
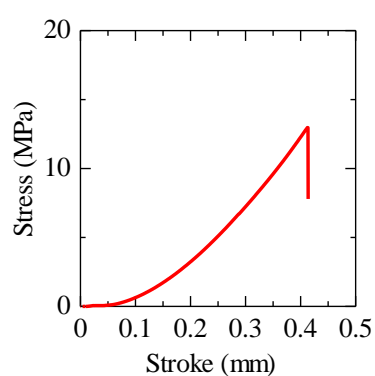
FWQ Sample No. 17
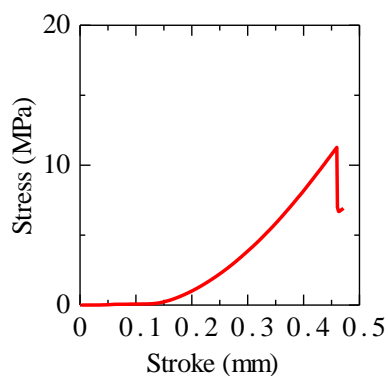
FWQ Sample No. 18
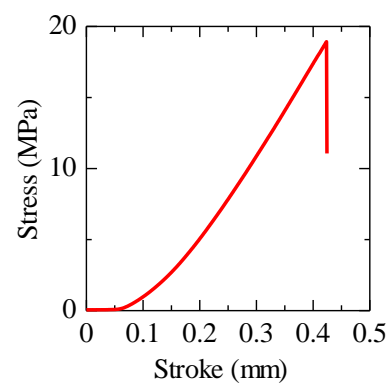
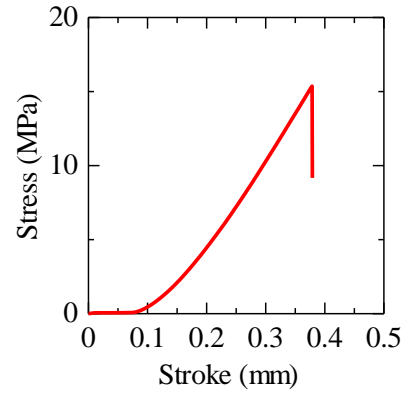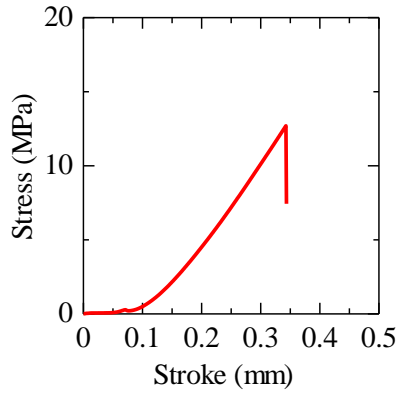FWQ Sample No. 19

FWQ Sample No. 22

FWQ Sample No. 24

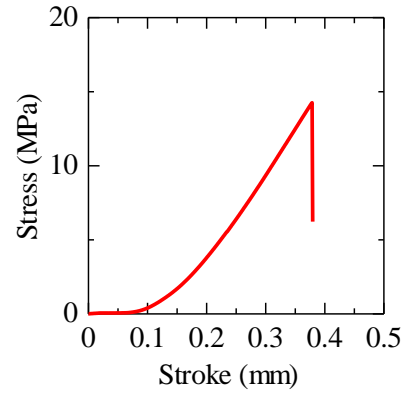Fig 3.4 Stress-stroke graphs for footwall quartzite test samples.

OBQ Sample No. 14

OBQ Sample No. 15

OBQ Sample No. 18

OBQ Sample No. 19

Fig 3.5 Stress-stroke graphs for orebody quartzite test samples.

3.3 Uniaxial compression test

3.3.1 Methods

Uniaxial compression test was conducted on the specimens using an Instron loading frame as shown in Fig 3.6. The specimens had approximate dimensions of diameter 30 mm and length 60 mm. The test was conducted at a strain rate of 10^{-4} s^{-1}. Correction on the UCS for specimen size was applied, using Eq. (3.2) as proposed by Hoek and Brown (1980).

$$\frac{\sigma_{50}}{\sigma_n} = \left(\frac{D}{50}\right)^{0.18} \tag{3.2}$$

Where σ_{50} is the UCS of a 50mm diameter specimen, σ_n is the UCS of a specimen with different diameter, and D is diameter of the specimen. The tangent modulus was corrected in the same way (E_{50r}).
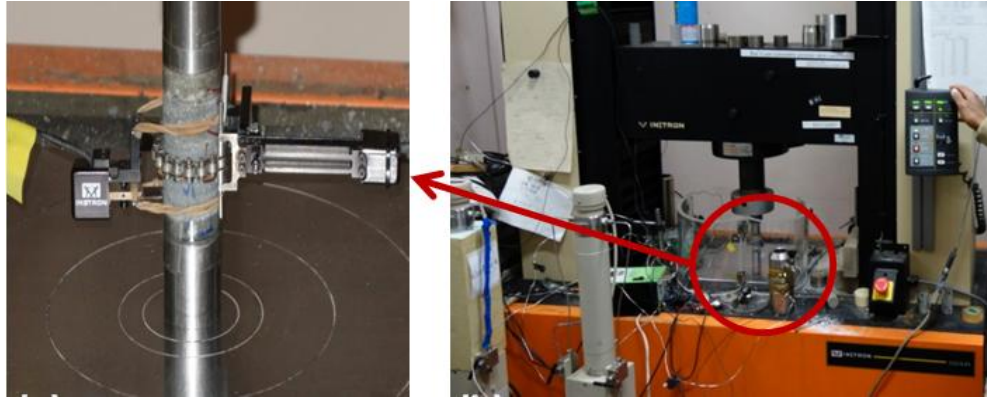
Fig 3.6 Experiment set up for UCS test, (showing the Instron loading frame, and the specimen and extensometer arrangement).

3.3.2 Results

The results of this test are provided in Tables 3.3 and 3.4. Fig 3.7 and 3.8 show the stress-strain curves obtained from this test.

Table 3.3 Mechanical properties of orebody quartzite.

| OBQ Sample No.	σ_n (MPa)	σ_{50} (MPa)	E_r (GPa)	E_{50r} (GPa)	Poisson's ratio
3	259	236	69.2	63.1	0.192
4	223	203	70.9	64.7	0.280
7	265	242	69.8	63.7	0.216
11	263	240	67.9	61.9	0.276
Average	253 ± 20	230 ± 18	69.5 ± 1.3	63.3 ± 1.1	0.241 ± 0.044

Table 3.4 Mechanical properties of footwall quartzite.

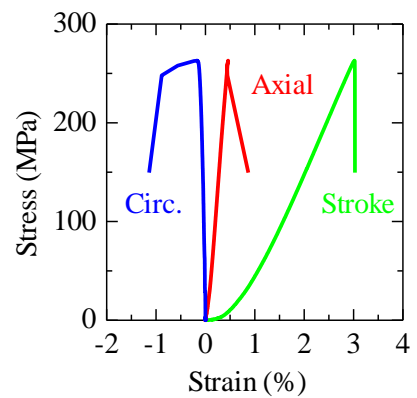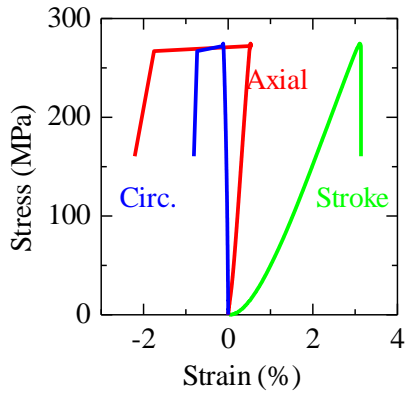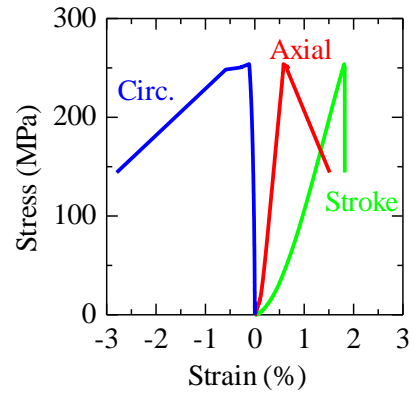| FWQ Sample No.	σ_n (MPa)	σ_{50} (MPa)	E_r (GPa)	E_{50r} (GPa)	Poisson's ratio
4	275	251	61.3	55.9	0.241
5	254	232	53.0	48.3	0.188
9	245	223	62.7	57.2	0.244
10	283	258	60.0	54.7	0.247
14	271	247	51.0	46.5	0.188
Average	266 ± 16	242 ± 14	57.6 ± 5.3	52.5 ± 4.8	0.222 ± 0.031
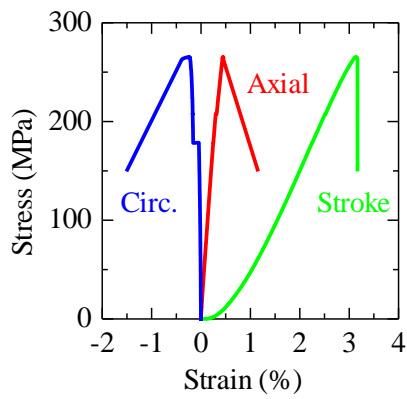
OBQ Sample No. 7
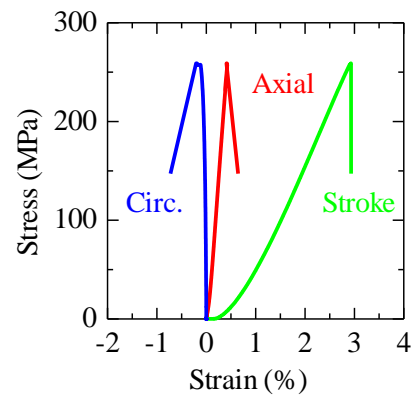
OBQ Sample No. 3
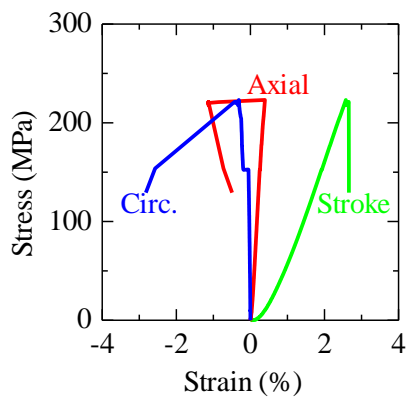
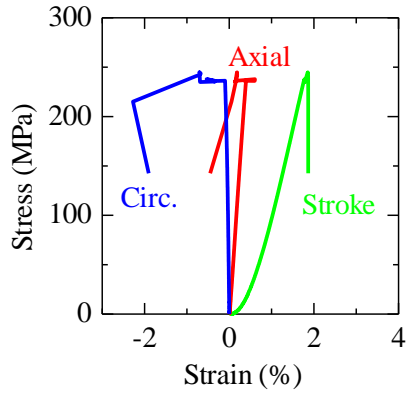OBQ Sample No. 4

OBQ Sample No. 11

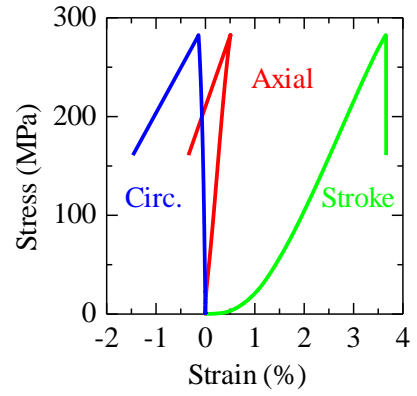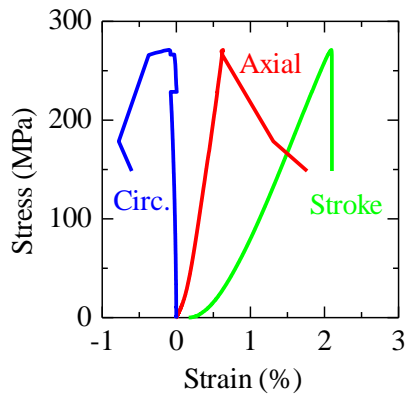Fig 3.7 Stress-strain curves for orebody quartzite samples.

FWQ Sample No. 4

FWQ Sample No. 5

FWQ Sample No. 9

FWQ Sample No. 10

FWQ Sample No. 14

Fig 3.8 Stress-strain curves for footwall quartzite sample.

3.4 Triaxial test

To further understand the mechanical properties of rocks at Mufulira Mine, triaxial tests were conducted on both orebody quartzite and footwall quartzite specimens, with specimen dimensions of approximately 60 mm length and 30 mm diameter.

3.4.1. Methods

The tests were conducted on an MTS loading frame as shown in Fig 3.9. For each rock type, five specimens were used, and each specimen set to one value of confining pressure among the values; 1 MPa, 5 MPa, 10MPa, 15 MPa and finally 20MPa.

Fig 3.9 Experiment set up for triaxial test, (showing the MTS loading frame, Hokkaido University).

Calculations were done for internal friction angle and friction angle on rupture plane using the expressions below, Eqs. (3.3) and (3.4) respectively.

$$\sigma_1 = UCS + \left(\frac{1 + \sin \phi}{1 - \sin \phi} \right) \sigma_3 \tag{3.3}$$

$$\sigma'_1 = \left(\frac{1 + \sin \phi'}{1 - \sin \phi'} \right) P_C \tag{3.4}$$

Where, σ_1 is peak strength, ϕ is internal friction angle, ϕ' is friction angle on rupture plane, P_C and σ_3 represent confining pressure and σ'_1 is residue strength.

3.4.2 Results

Tables 3.5 and 3.6 give a summary of the measurement results of the triaxial tests. The stress-strain curves for both orebody quartzite and footwall quartzite samples are shown in Fig 3.10 and 3.11. A relationship between axial

stress and confining pressure is illustrated in Fig 3.12, for both orebody quartzite and footwall quartzite test samples. The results on friction angles and residual strength are provided in Table 3.7.

Table 3.5 Measurement results of triaxial tests on orebody quartzite specimens.

OBQ Sample No.	Weight (g)	Length (mm)	Diameter (mm)	Confining pressure, σ_3 (MPa)	Peak stress, σ_1 (MPa)	Residue strength	Tangent modulus (GPa) (slope at 40-60% strength)
1	115.5	59.6	29.9	1	143	84.9	10.8
10	113.6	59.7	29.6	5	351.3	91.5	22.5
13	114.8	60.4	29.9	10	301	124.7	18.6
12	114.2	59.9	29.9	15	521.3	167.4	27.4
5	115	59.6	29.8	20	540	-	20.1

Table 3.6 Measurement results of triaxial tests on footwall quartzite specimens.

FWQ Sample No.	Weight (g)	Length (mm)	Diameter (mm)	Confining pressure σ_3 (MPa)	Peak stress σ_1 (MPa)	Residue strength	Tangent modulus (GPa) (slope at 40-60% strength)
12	109.9	59.5	29.4	1	220.2	32.4	19.9
1	108.9	59.9	29.7	5	219.6	85	15.8
6	110.2	59.5	29.8	10	208.1	150.1	15.7
3	110	60.3	29.5	15	355	219.9	15.9
2	108.9	59.9	29.6	20	430.2	220.1	21.9
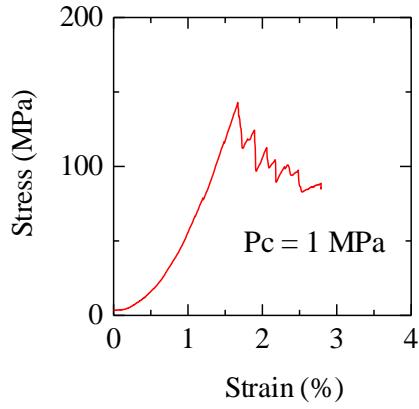
OBQ Sample No. 1
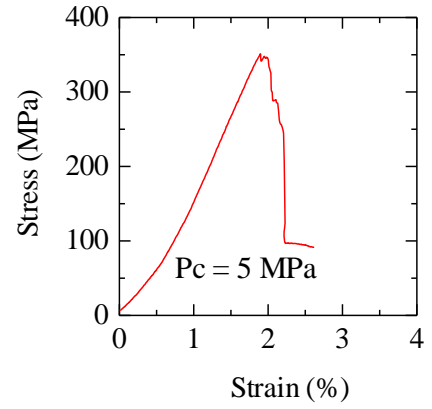
OBQ Sample No. 10
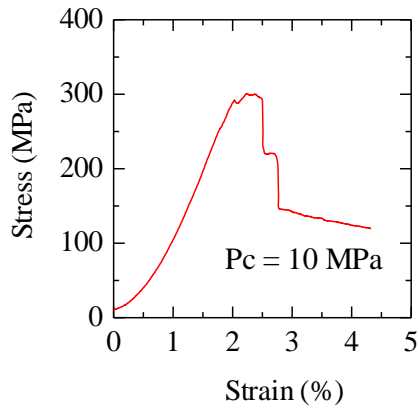
OBQ Sample No. 13

OBQ Sample No. 12

OBQ Sample No. 5

Fig 3.10 Stress-strain curves for orebody quartzite samples.

FWQ Sample No. 12
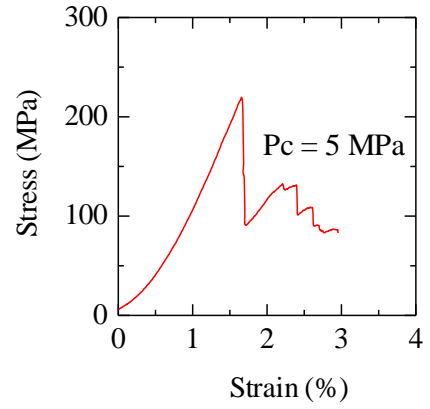
FWQ Sample No. 1
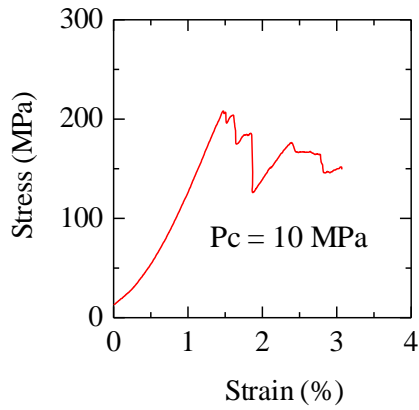
FWQ Sample No. 6
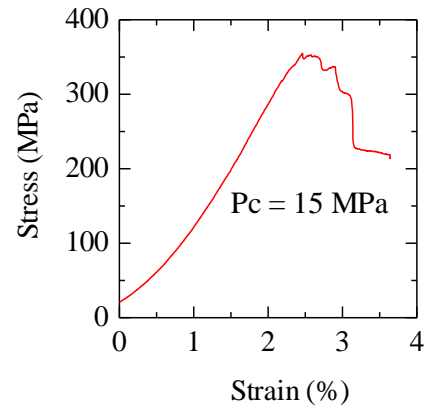
FWQ Sample No. 3
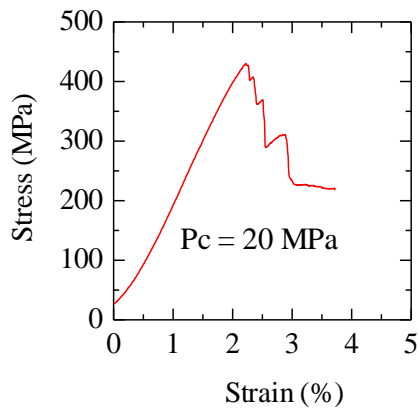
FWQ Sample No. 2

Fig 3.11 Stress-strain curves for footwall quartzite samples.
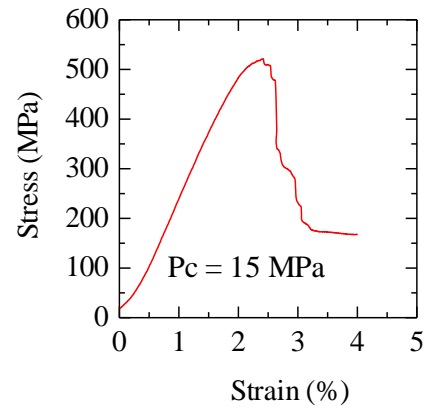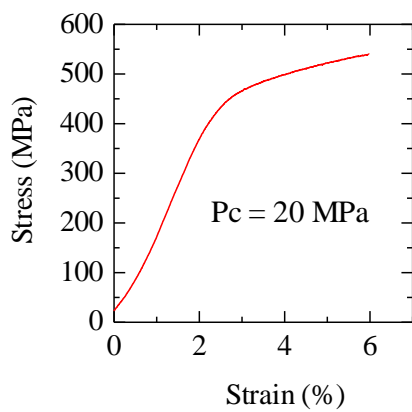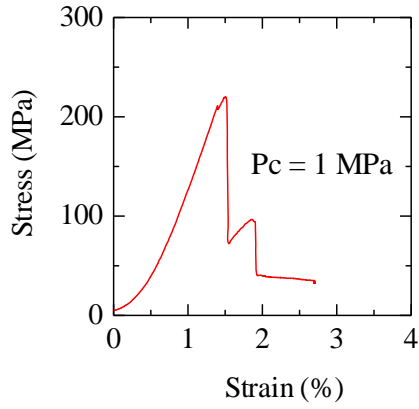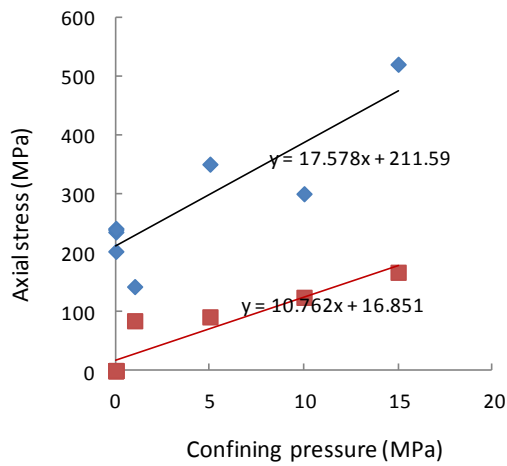
(a) Combined with UCS (for orebody quartzite)   (b) Without UCS (for orebody quartzite)
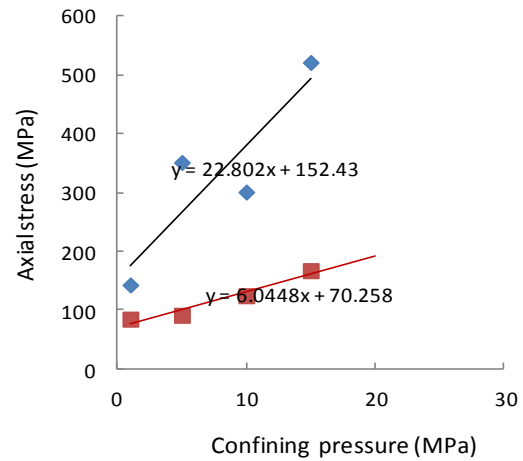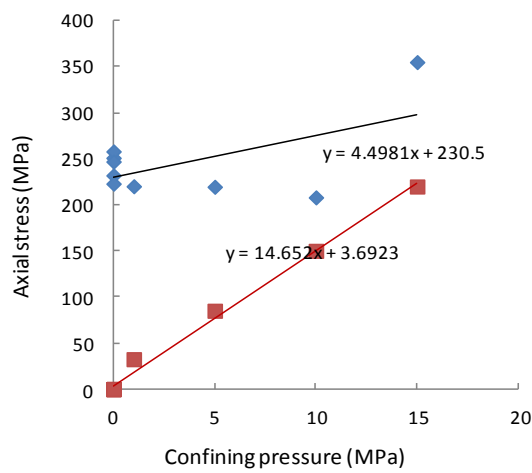
(d) Combined with UCS (for footwall quartzite)   (e) Without UCS (for footwall quartzite)
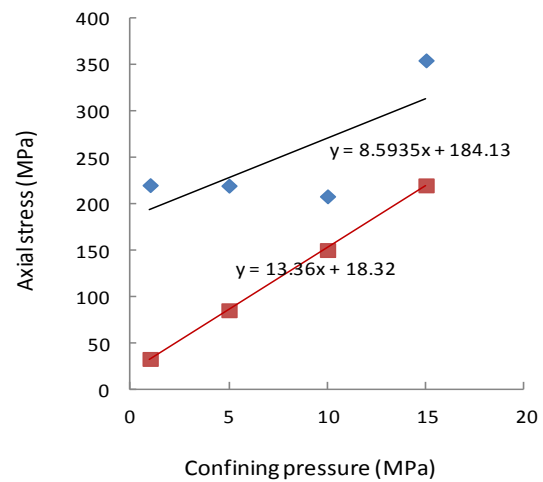
Fig 3.12 Axial stress (MPa) against confining pressure (MPa) graphs for orebody quartzite and footwall quartzite test samples.

Table 3.7 Friction angles and residual strength from triaxial test.

Sample	UCS (MPa)	Cohesion (MPa)	Internal friction angle, ϕ (°)	Residual strength (MPa)	Friction angle on rupture plane, ϕ' (°)
OBQ	211.6	25.2	63.2	16.9	56.1
FWQ	230.5	54.3	39.5	3.7	60.7

4. Stress analysis

4.1 Mine-wide stress analysis by 3D DDM

4.1.1 Method

The initial model was developed following the layout of the Mufulira mine as of July 2016 (Fig. 4.1). The area was divided into 3.0 m × 3.0 m square elements. The model is extracted from mining blocks 60 to 66 along the strike direction and from 1357-1473 m level in depth at the main mine, covering 600 m in length. It was extracted by 374 mining steps with a 3.0 m face advance/step. Fujii et al. (1997) and Fujii et al. (2001) explained the conceptual equations applied in this method.
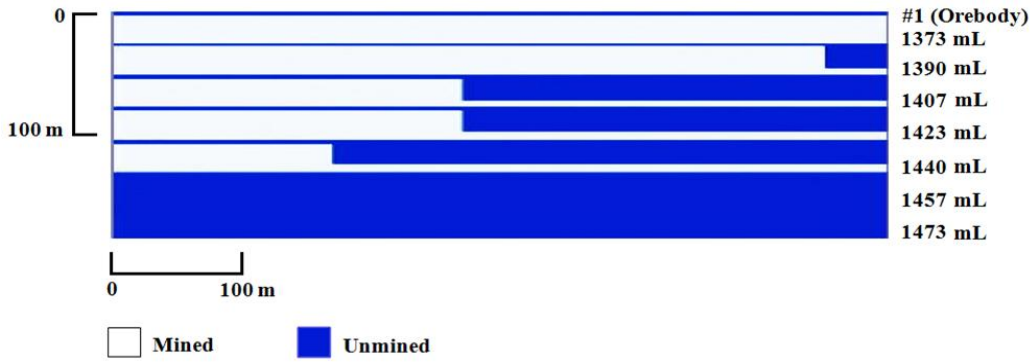
Fig. 4.1 Input model for the numerical analysis (the mine layout as of July 2016).

Assuming a fracture normal to the x_3-direction (Fig. 4.2), the displacement discontinuity b_1 and b_2 represent shear slip between the fracture surfaces in the x_1 or x_2 direction, whereas positive or negative b_3 represents opening or closure of the fracture. The displacement and stress components, u and σ at an arbitrary point Q can be represented as

$$u_m = b_k \iint_\Sigma T_k^m d\Sigma \tag{4.1}$$

$$\sigma_{mn} = b_k W_k^{mn}$$
$$W_k^{mn} = \iint_\Sigma H_k^{mn} d\Sigma \tag{4.2}$$

where

$$T_k^m = \frac{1}{4\pi}\left\{(1-\alpha)\left(-\delta_{k3}\frac{r_m}{r^3}+\delta_{mk}\frac{r_3}{r^3}+\delta_{3m}\frac{r_k}{r^3}\right)+3\alpha\frac{r_k r_m r_3}{r^5}\right\}$$

$$\alpha = \frac{\lambda+\mu}{\lambda+2\mu}$$

$$H_k^{mn} = \lambda\delta_{mn}T_k^{h,h} + \mu(T_k^{m,n}+T_k^{n,m}) \tag{4.3}$$

$$T_k^{m,n} = \frac{\partial T_k^m}{\partial \xi_n}$$

δ : Kronecker delta, λ and μ: Lamé's constants

$r_k = x_k - \xi_k$ and $r = \sqrt{r_k r_k}$

(Salamon, 1964).
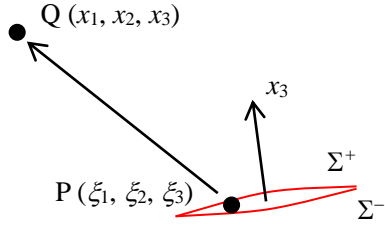
Fig. 4.2 A displacement discontinuity element with a point P on the element and an arbitrary point Q.

For a case for a tabular ore seam normal to x_3 direction, the seam is divided by displacement discontinuity elements and the boundary conditions for mined elements are assigned as

$$\tau_{zx} = \tau_{xy} = \sigma_z = 0 \tag{4.4}$$

where τ is the shear stress. If $-b_3$ exceed the working height t,

$$b_3' = -t \tag{4.5}$$

and

$$b_1' = b_1 \frac{b_3'}{b_3}$$

$$b_2' = b_2 \frac{b_3'}{b_3} \tag{4.6}$$

(Crouch and Fairhurst, 1973). However,

If $\tau_{max} = \sqrt{\tau_{zx}^2 + \tau_{yz}^2} \geq -\sigma_z \tan\phi,$

$$\tau_{zx}' = \tau_{zx} \frac{-\sigma_z \tan\phi}{\sqrt{\tau_{zx}^2 + \tau_{yz}^2}} \tag{4.7}$$

$$\tau_{xy}' = \tau_{yz} \frac{-\sigma_z \tan\phi}{\sqrt{\tau_{zx}^2 + \tau_{yz}^2}}$$

where ϕ is the friction angle. For unmined elements,

$$\tau_{xz} = \frac{b_1}{t} G$$

$$\tau_{yz} = \frac{b_2}{t} G$$

$$G = \frac{E}{2(1+v)} \tag{4.8}$$

$$\sigma_z = \frac{b_3}{t} E$$

where G, E, and v are the shear modulus, Young's modulus and Poisson's ratio, respectively. Displacement discontinuity values can be obtained by formulating and solving the above equations for all elements.

38

Displacement and stress at arbitrary points can be obtained from the displacement discontinuity values.

In the 3-D FEM by Sepehri et al. (2020), 0.4-1.5 million elements and around 60 mining steps were used. For comparisons, the DDM model in this study consists of 200 x 56 elements with 374 mining steps. The number of elements may seem too small for a modern analysis. However, DDM is a boundary element model in an infinite elastic medium, and only the ore body is divided. FEM would instead require both the hanging wall and footwall to be divided. Using 3-D FEM instead of DDM would at least need 200 x 56 x 56 = 0.6 million elements, which is within the range carried out by Sepehri et al. (2020). The computing load would then be approximately six times more because of this study's larger number of mining steps. Our model's 3.0 m x 3.0 m resolution is also not too coarse compared to the coarsest element size of 110 m in Sepehri et al. (2020).

The lithostatic state of stress was assumed for simplicity, as illustrated in Eq. (4.9).

$$\sigma_v = \sigma_H = \sigma_h = \gamma h \tag{4.9}$$

where σ_v is the vertical component of stress, σ_H is the maximum horizontal stress, σ_h is the minimum horizontal stress, γ is the unit weight of the rock mass, and h is the overburden depth. The rock mass unit weight was assumed as 27 kN/m^3 (Table 4.1). The average value of Poisson's ratio from the rock tests in Table 3.3 and 3.4 was used. The corrected values of tangent modulus were obtained using Eq. (4.10) (Zhang and Einstein, 2004), considering the average value of RQD as 64.5% for 1457 and 1423 m levels.

$$E_m = 10^{0.0186RQD-1.91} E_r \tag{4.10}$$

where E_r is the rock specimen tangent modulus, and E_m is the rock mass tangent modulus.

Table 4.1 Input parameters for numerical analysis.

Rock	Unit weight (N/m^3)	Tangent modulus (GPa)	Poisson's ratio
Hanging wall and footwall	27,000	12.33	0.222
Orebody	27,000	10.23	0.241

DDM considers closure of the tabular mined out areas, and induced stress usually decreases with decreasing elastic moduli in longwall coal mining cases. It increases with elastic moduli and converges to the elastic solution without closure. Hindcasting such observations can adjust the tangent modulus values as surface subsidence and underground displacement. However, this study obtained no closure because of the thicker orebody, higher tangent modulus, and shorter unsupported span than longwall coal mining. Therefore, elastic constants do not affect the stress distribution for this case, although the ratio of elastic constants may slightly affect the stress distribution. The thin inclusion was removed as the mining status of elements at the mining face

was changed from "unmined" to "mined" in a mining step in which the face advances by the element length of 3 m in strike direction.

For more accurate stress analysis, there is need to consider the ratio of horizontal stress to vertical stress. In Zambia, the maximum horizontal stresses are generally in the NE-SW direction (Fig. 4.3). However, so far there are no reports or observations that show apparent strong tectonic stress from NE. Therefore, and for simplicity, the hydrostatic state of stress was assumed (Eq. 4.9). In future, the effect of initial stress will be considered more accurately.

(a)   (b)
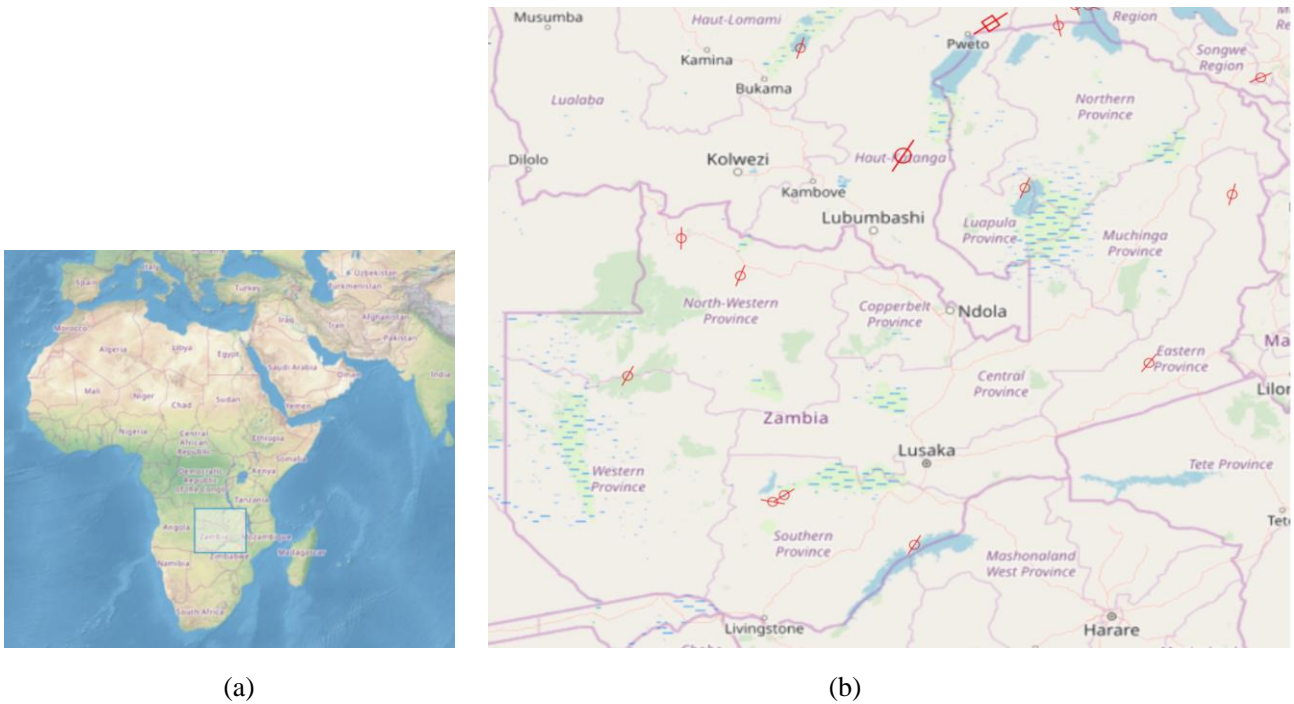
Fig. 4.3 Maximum horizontal stresses: (a) map extraction of Zambia and (b) preview of directions of maximum horizontal stresses. Data source: https://www.world-stress-map.org/casmo.
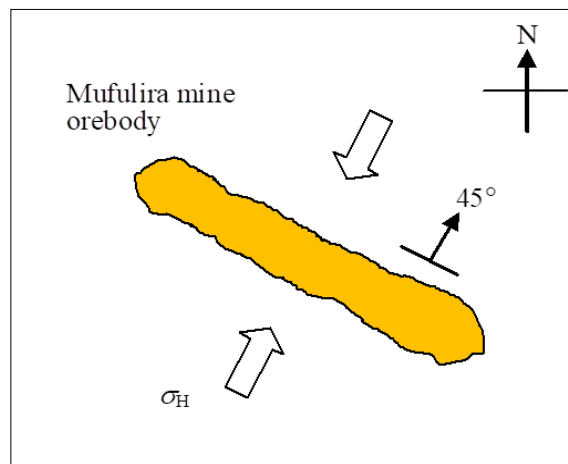
Fig. 4.4 The maximum horizontal stresses are directed perpendicularly to the Mufulira mine orebody.

40

4.1.2 Results

The normal stress distribution on the ore body is shown in Fig. 4.5. It should be worth noting that the calculated normal stress is for the center of each 3.0 m × 3.0 m element, and the sidewall stress would be slightly higher than the normal stress. Based on the analysis, it was observed that the highest concentration of stress was in the chain pillars.

(a) #1 and #2

(b) #4, #5 and #6

(c) #8

(d) #9

(e) #10

(f) #12
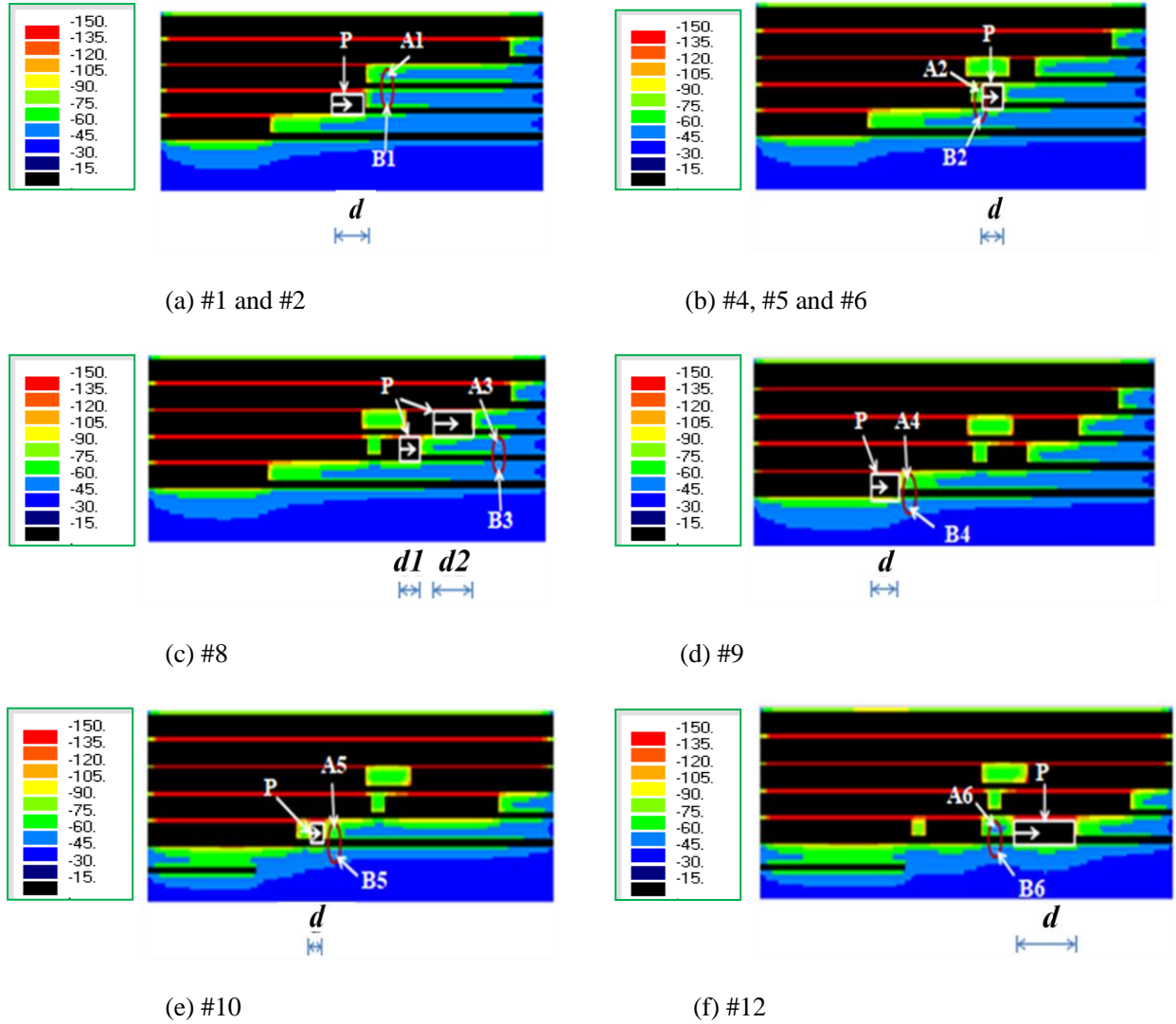
60m

Fig. 4.5 Changes in the distribution of normal stress (MPa) on the ore body due to face advance (P: stope extracted before rockburst, d: face advance, A1-A6: south-west side, B1-B6: north-east side of rockbursts).

The stress component normal to the sidewall is not properly calculated because DDM approximates the mining drives by the thin displacement discontinuity elements, and the free surface condition on the sidewall is not

41

considered in the model. That is one of the shortcomings of DDM. However, the component is effectively zero at the edge element (Fig. 4.6), unmined but next to the mined element. High uniaxial stress concentration due to mining appears on the edge elements. Rock mass failure can occur everywhere around mining areas. However, failure inside the rock mass, for which triaxial stress state should be considered, is just a microseismic event. On the other hand, rock mass failure, which occurred at or near the free surface where the minimum principal stress is either zero or small, can be recognized as rockburst. That is why only the normal stress component acting on the orebody is shown.

(a) Plan view   (b) Section view
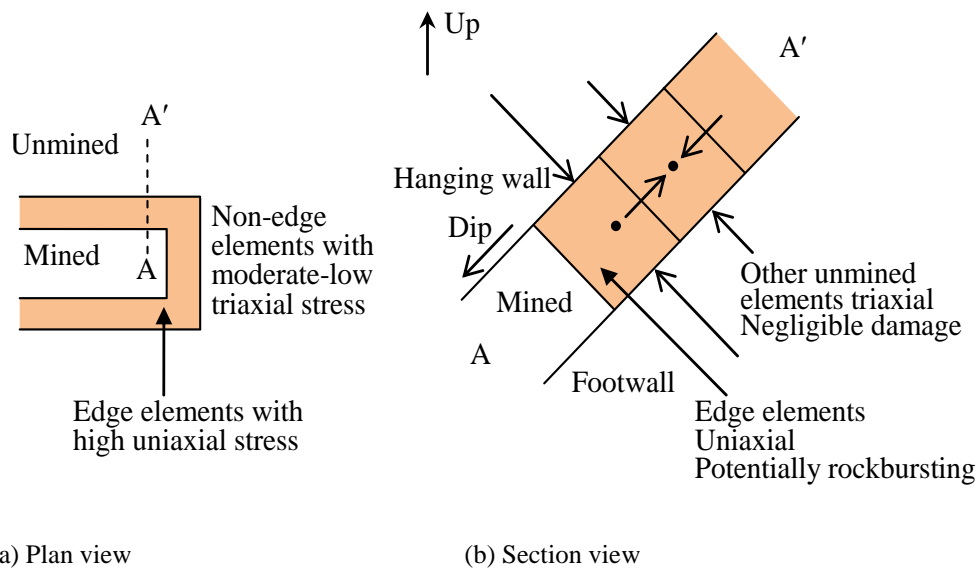
Fig. 4.6 Concept of edge element.

As mine extraction advances, the normal stresses increase around the excavation (Fig. 4.7). It was confirmed that the stress level at the rockbursts #4, #5, and #6 (Figs. 4.5b and 4.7b) significantly increased with face advance because the site is at a narrow pillar. The stress for event #9 (Figs. 4.5d and 4.7d) also significantly increased because the site is near the mining face.

On the other hand, stress only slightly increased at the sites for events #1 and #2 (Figs. 4.5a and 4.7a), and #8 (Figs. 4.5c and 4.7c) rather far ahead of the face. The stress increase for event #10 (Figs. 4.5e and 4.7e) is slight because the panel length is short. The stress increase for event #12 is small despite the site being at a pillar because the pillar is relatively wide. There are no apparent positive correlations between rockburst occurrences and the stress value before the mining, just before the rockburst, or stress increment by mining, as shown by the low coefficients of correlation in Fig. 4.8. It seems difficult to explain rockburst occurrences only from the normal stress behavior by DDM.
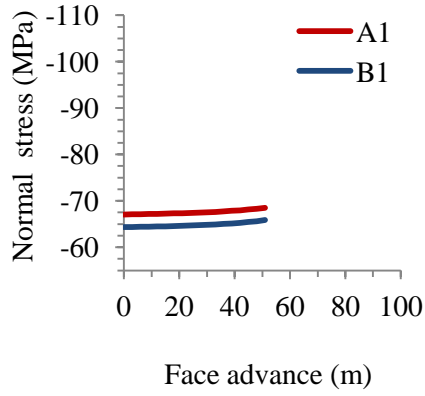
(a) For #1 and #2
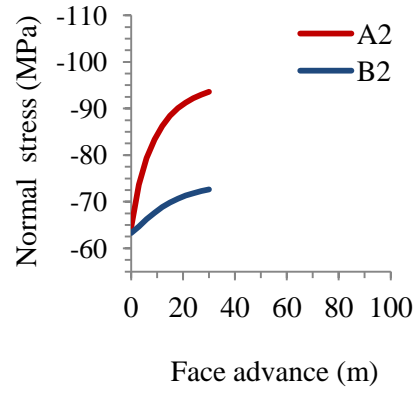
(b) For #4, #5 and #6
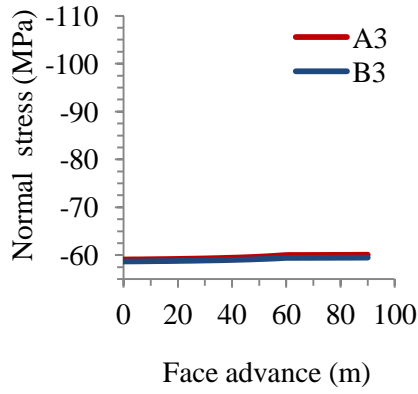
(c) For #8
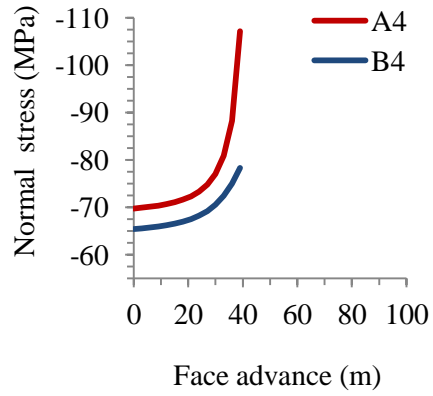
(d) For #9
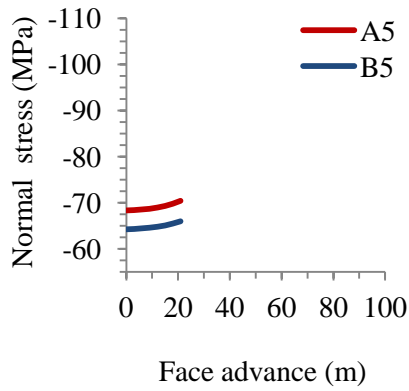
(e) For #10
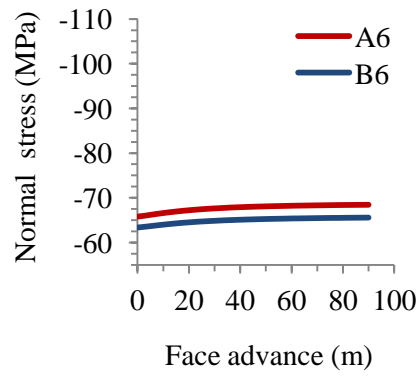
(f) For #12

Fig. 4.7 Changes in the normal stress due to face advance at rockburst sites. See Fig. 4.5 for A1-A6 and B1-B6.

43
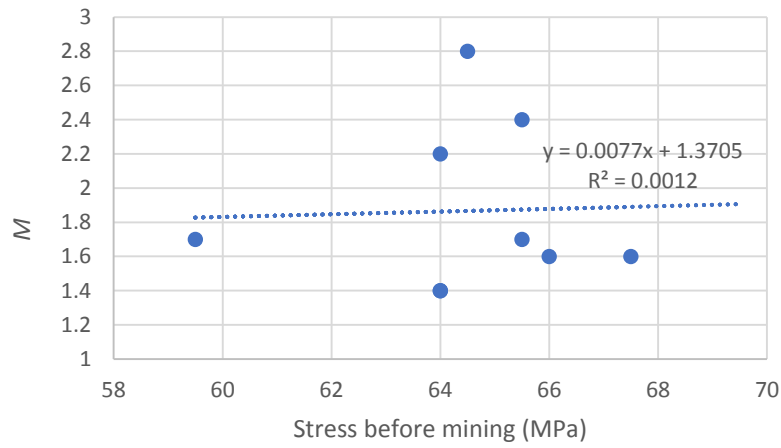
(a) Before mining (initial value of Fig. 4.7)
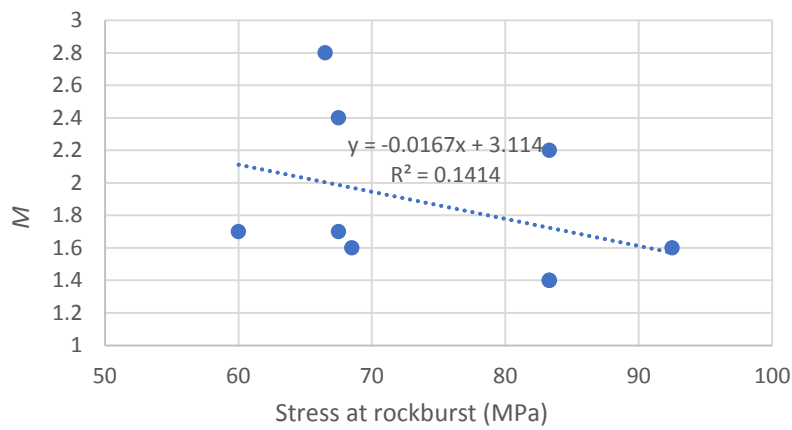
(b) Just before rockbursting (final value of Fig. 4.7)
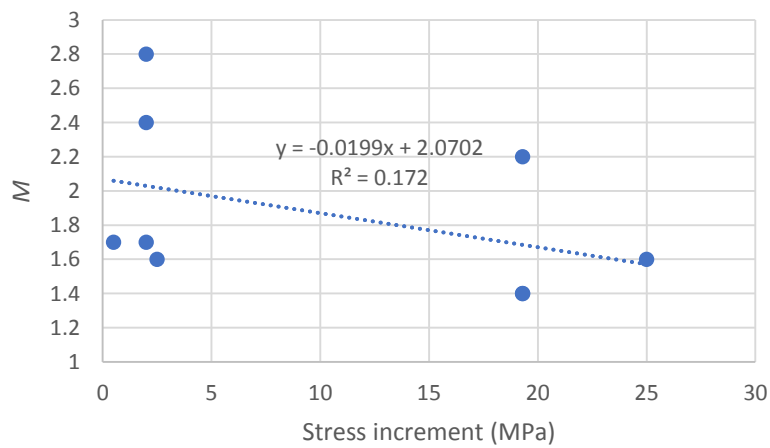
(c) Increment by mining (from the initial to the final value of Fig. 4.7)

Fig. 4.8 Normal stress value at the rockburst sites and the magnitudes of rockbursts (average of stress values at A and B in Fig. 4.7).

4.2 Stress analysis on rockburst sections by 2D FEM

4.2.1 Method

4.2.1.1 2D FEM model

DDM cannot precisely calculate all the stress components in the vicinity of the mining drives as described above. However, DDM can give the degree of stress concentration by mining. Therefore, a more precise elastic stress distribution on the rockburst sections was calculated by 2-D FEM applying the concentrated stress by mining.

The normal displacements at the left and the bottom were confined, and isotropic stresses were applied from the top and the right boundaries (Fig. 4.9). The stress value was adjusted so that average normal stress on the orebody 4.5 m away from the center of the mining drive up and down dipward becomes identical to the DDM results for simplicity. The same mechanical properties as DDM were used.
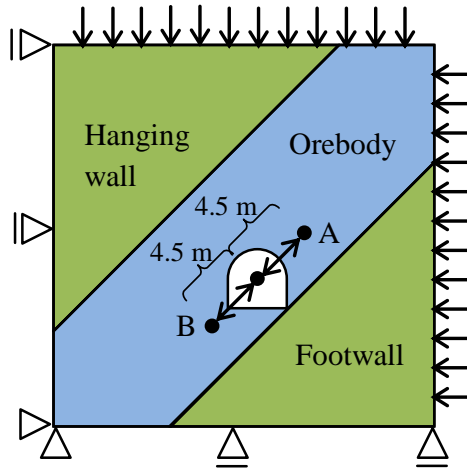
Fig. 4.9 2-D FEM model at the rockburst section.

Cases for rockbursts #9 and #12 were selected. The former is located near the face, and the normal stress was significantly increased by the mining (Fig. 4.7d). The latter is located behind the starting entry of the stope, and the normal stress showed almost no increase (Fig. 4.7f).

4.2.1.2 Modified stress severity

In order to represent the relative level of the calculated stress state, the unique modified stress severity S_S was proposed and used (Fig. 4.10). The stress severity for compressive failure can be defined as

$$S_{SC} = \frac{R*}{R} = \frac{\sigma_1 - \sigma_3}{\text{UCS} + \alpha\sigma_3 - \sigma_3}$$

(4.11)

45

$$\alpha = \frac{1+\sin\phi}{1-\sin\phi}$$

(4.12)

where σ_1 and σ_3 are the maximum and minimum principal stresses respectively. For tensile failure, it is defined as

$$S_{ST} = \frac{\sigma_3}{T_0}$$

(4.13)

If $-\sigma_3 \geq T_0$ or $S_{SC} < -S_{ST}$, then

$$S_S = S_{ST}$$

(4.14)

Or, if $S_{SC} > -S_{ST}$,

$$S_S = S_{SC}$$

(4.15)
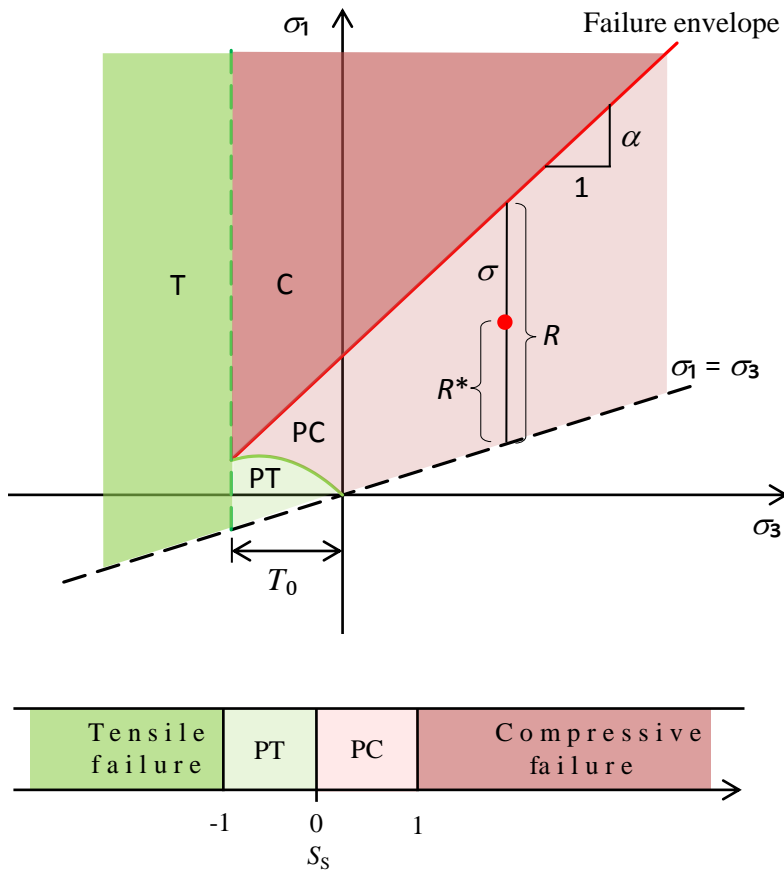
Fig. 4.10 Modified stress severity for arbitral stress state. T: tensile, C: compressive, PT: potentially tensile, and PC: potentially compressive failure.

This modified stress severity is useful because only one index can be used for compressive and tensile failure. Namely, the positive/negative stress severity indicates the possibility of compressive/tensile failure, and the

46

modified stress severity of 1/−1 indicates that the stress state reaches the compressive/tensile failure criterion (Fig. 4.10). More precisely, the boundary between potentially compressive and tensile failure is represented from Eqs. (4.11) and (4.13) as

$$\sigma_1 = \left(1 - \frac{UCS}{T_0}\right)\sigma_3 - \frac{\alpha - 1}{T_0}\sigma_3^{\,2}$$

(4.16)

(see Fig. 4.10). The parameters in Tables 2 and 4 were corrected similar to the tangent modulus correction, substituting the average RQD of 64.5% into Eq. (4.10) and used to evaluate the modified stress severity (Table 4.2).

Table 4.2 Strength parameters for evaluation of stress severity.

Rock	UCS (MPa)	Internal friction angle, ϕ (°)	Tensile strength, T_0 (MPa)
Hanging wall and footwall	45.0	39.5 → 30	2.6
Orebody	41.3	63.2 → 30	2.5

4.2.2 Results

The maximum principal stress significantly increased due to mining for #9 (Fig. 4.11a to b) and slightly increased for #12 (Fig. 4.12a to b). However, the results showed a small region with more than one stress severity even for #9 (Fig. 4.11e to f). The internal friction angles of 39.5° and 63.2° are obtained from the triaxial test (Table 4.2); however, those values are higher than the typical range of internal friction angles for metamorphic sedimentary rocks. Therefore, the calculation for stress severity around mining drives was repeated for #9 and #12 with an internal friction angle of 30°. Stress severity slightly increased for rockburst #9 (Fig. 4.11g to h) and no increase for #12 (Fig. 4.12e to f). The meshing is coarse; only elastic analysis was carried out, and the boundary condition was simplified. However, significant yield zones and their growth by stress increase due to mining would not be expected for both rockbursts even if an elasto-plastic analysis was conducted with a finer meshing under precisely reconstructed boundary conditions.
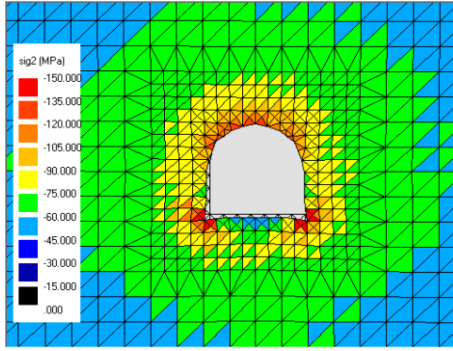
(a) Maximum principal stress before mining   (b) Just before rockburst
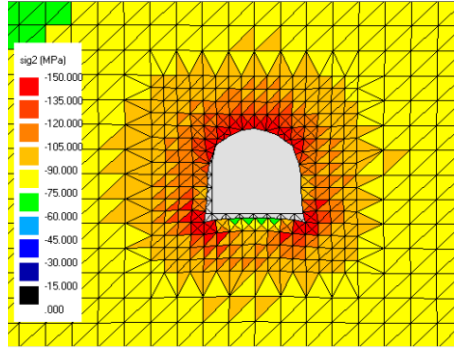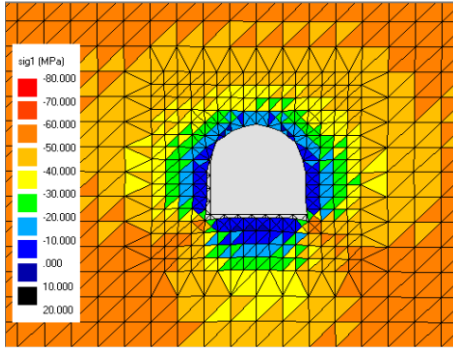
(c) Minimum principal stress before mining   (d) Just before rockburst
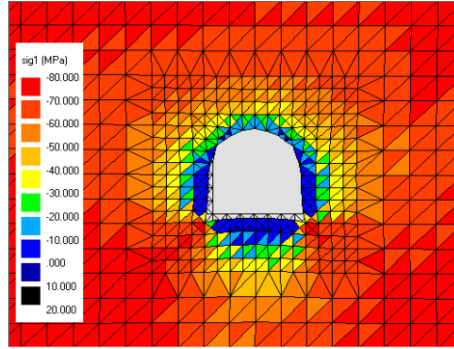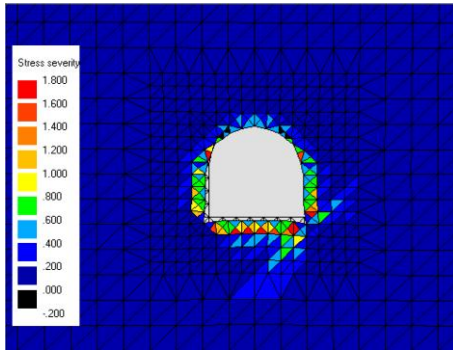
(e) Modified stress severity before mining,
    $\phi = 39.5°$ (hanging wall) and $63.2°$ (orebody)
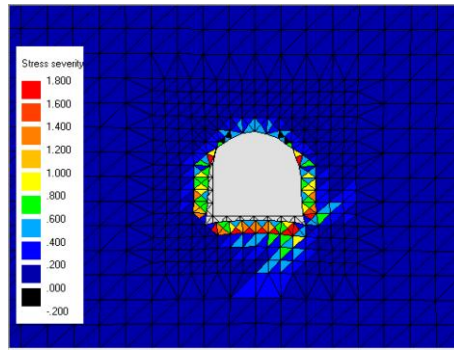
(f) Just before rockburst
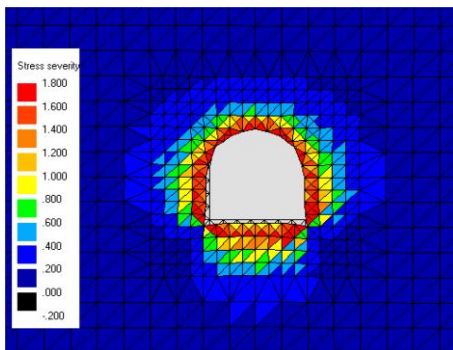
(g) Modified stress severity before mining, $\phi = 30°$ (h) Just before rockburst
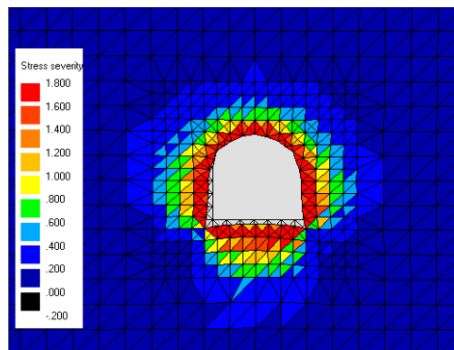
Fig. 4.11 Results of FEM for #9 (compressive stress is in negative and the displacement was magnified 10 times).
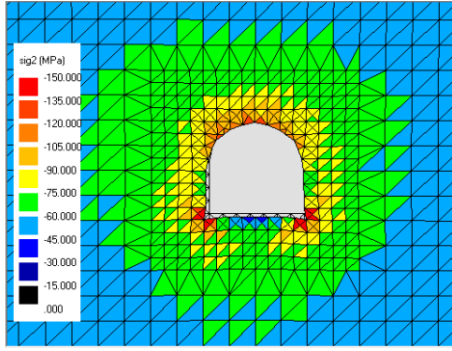
(a) Maximum principal stress before mining   (b) Just before rockburst
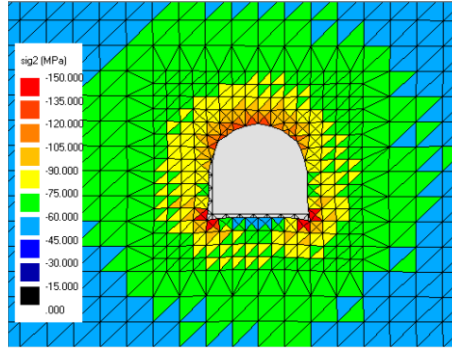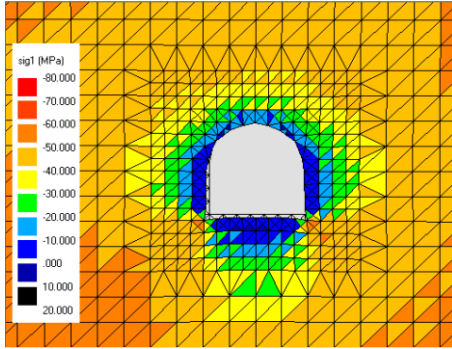
(c) Minimum principal stress before mining   (d) Just before rockburst
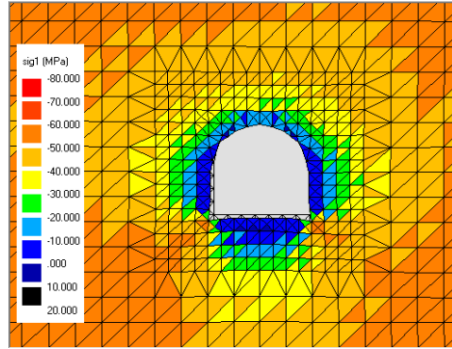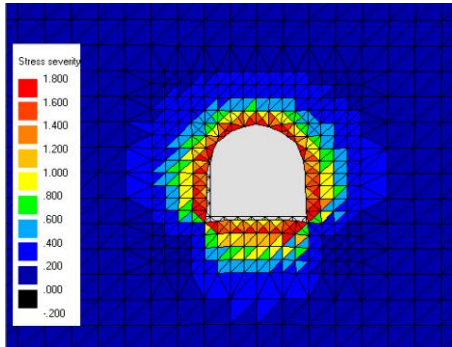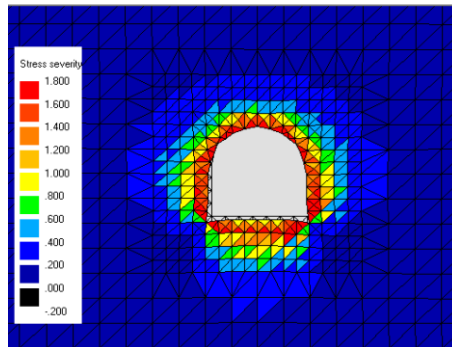
(e) Modified stress severity before mining   (f) Just before rockburst

Fig. 4.12 Results of FEM for #12, $\phi = 30°$ (compressive stress is in negative and the displacement was magnified 10 times).

5. Creep damage model

5.1 Concept of brittle creep failure

The relatively wide area of rock mass left around the M2.8 behind the starting entry experiences moderate stress concentration (Fig. 4.7f), which may not reach instantaneous strength but exceed the long-term strength for creep failure over a long time (Fig. 5.1), and the rock mass has not been blasted for ore extraction within that period. That stress level may have been kept over a long time, and brittle creep failure may have finally occurred and then recognized as the severe rockburst. This similar characteristic was observed even for other rockburst cases. Therefore, a creep damage model as rockburst was proposed.
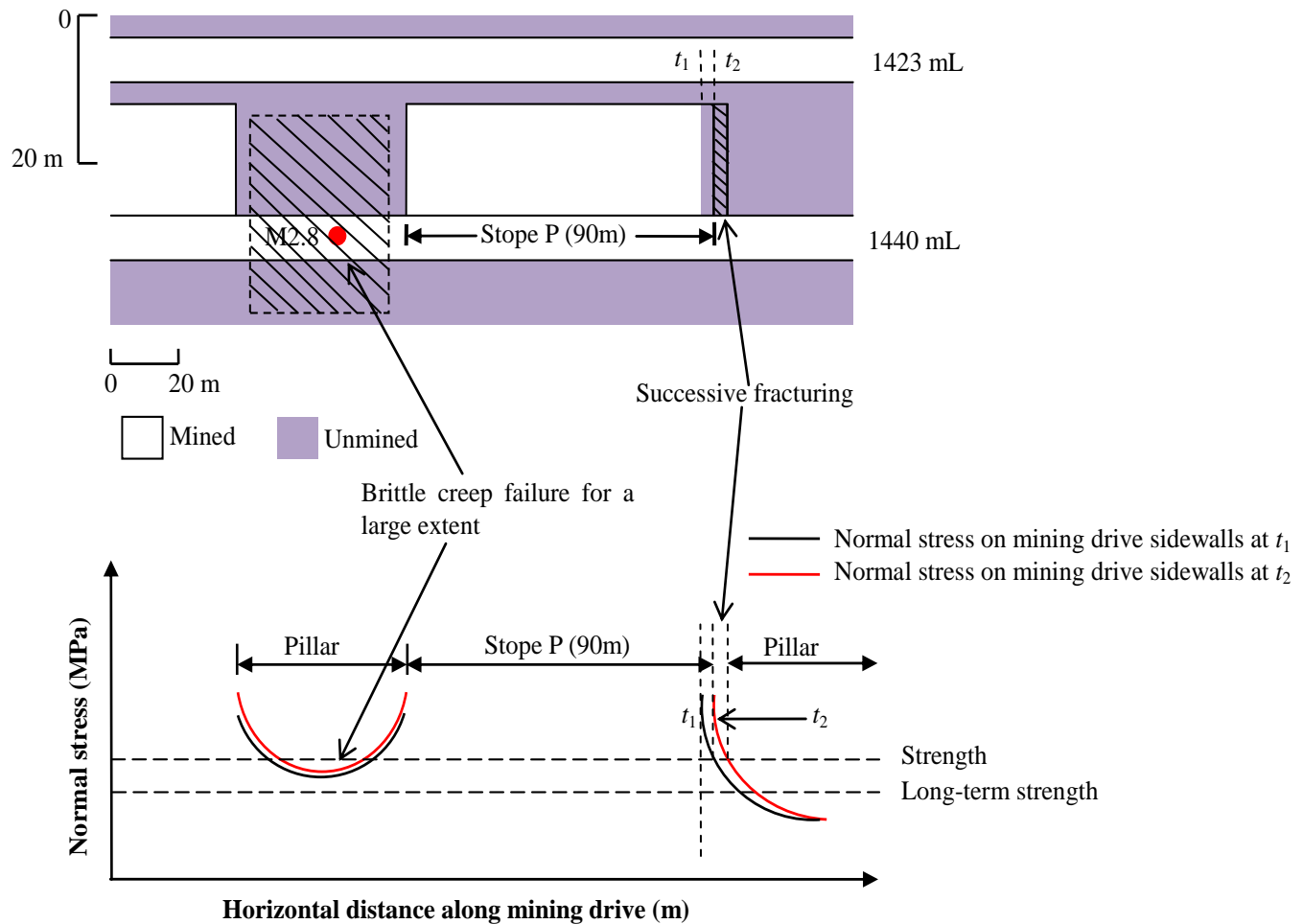
Fig. 5.1 Concept of rockburst as brittle creep failure of relatively intact rock mass under moderate stress for a long time.

Inada granite is a typical hard rock that showed creep failure (Fujii, 1999). Similarly, the Mufulira quartzite rocks would most likely show creep failure.

5.2 Method

The basic concept of the creep damage model on the rate of creep damage D is shown in Eq. 5.1, where S_{SC} is the stress severity for compressive failure. And n is a constant which represents the degree of time-dependency of strength.

$$\frac{dD}{dt} = S_{SC}^{n}$$

$$(5.1)$$

Assuming that rock mass failure occurs when D reaches 1, the time of failure under a constant stress severity is obtained as

$$t_{F} = S_{SC}^{-n}$$

$$(5.2)$$

or

$$\log(S_{SC}) = -\frac{1}{n}\log t_{F}$$

$$(5.3)$$

This equation represents the typical relationship between creep stress and time to failure (ex. Goodman, 1980) and t_F becomes 1 when $S_{SC} = 1$.

Rock damage was evaluated based on the normal stress obtained by the 3-D DDM. The calculation was carried out using the input parameters in Table 5.1, following the simulation procedure shown in Fig. 5.2. The mining speed was simplified to 3.0 m/day. The damage was calculated only for edge elements, which were unmined but next to the mined elements (Fig. 4.4). The edge elements are subjected to high uniaxial stress concentration. Therefore, much greater damage appears for the edge elements. However, it was confirmed that the other unmined elements further away from the edge were subjected to triaxial stresses, and their expected damage was negligible by a preliminary calculation. This finding stands as long as the elastic analysis is concerned.

Table 5.1 Input parameters for brittle creep model.

UCS (MPa)	n	Δt (Day)
80	$10 \rightarrow 40$	1
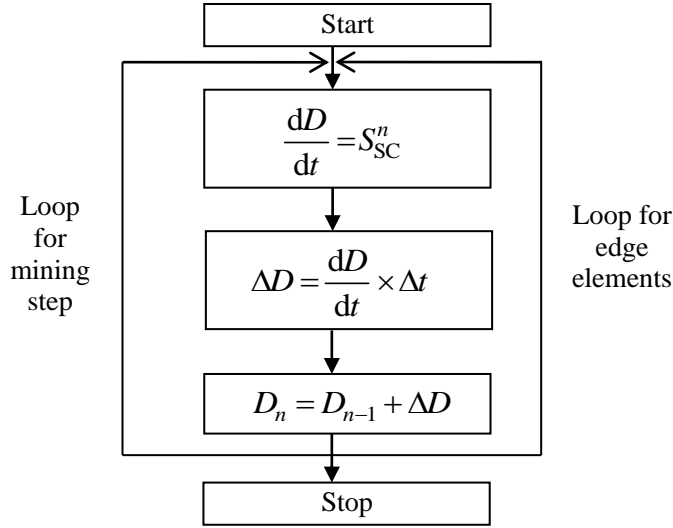
Fig. 5.2 Flow chart of the simulation program for damage (ΔD: damage increment in a mining step, Δt: time for a mining step, D_n: cumulative damage to the n-th mining step).

Lateral stress in the vicinity of the mined-out area is not precisely calculated by DDM but is needed to evaluate creep damage of non-edge elements. Fujii and Ishijima (1994) developed a method to evaluate lateral stress in the vicinity of the mined-out area by comparing DDM results to FEM results which can precisely estimate the lateral stress in the vicinity of the sidewall as

$$
\begin{aligned}
\sigma_{\mathrm{H}} &= B\frac{x}{t}, \text{ for } x \leq t \\
B &= 0.32\sigma_{\mathrm{VF}} + R_3\sigma_{\mathrm{H}}^0 \\
\sigma_{\mathrm{VF}} &= R_1\sigma_{\mathrm{V}h} \\
R_1 &= 1.25\left(\frac{h}{t}\right)^{0.753}\left(\frac{E_{\mathrm{O}}}{E_{\mathrm{R}}}\right)^{0.392} + 1 \\
R_3 &= -0.213\log\frac{E_{\mathrm{O}}}{E_{\mathrm{R}}} = 0.606
\end{aligned}
\tag{5.4}
$$

where σ_{H} is the lateral stress, x is the distance from the sidewall, t is the working height, σ_{VF} is the normal stress at the sidewall, σ_{H}^0 is the initial lateral stress, $\sigma_{\mathrm{V}h}$ is the stress at the center of the edge element, E_{C} is Young's modulus of the ore body and E_{R} is Young's modulus of the rock mass (Fig. 5.3).

Creep damage analysis starts at the initial model from 2016. The results may contain large errors, in particular for the first several ten steps around old workings. However, the results around the newly developed mining drives and mining panels would be okay
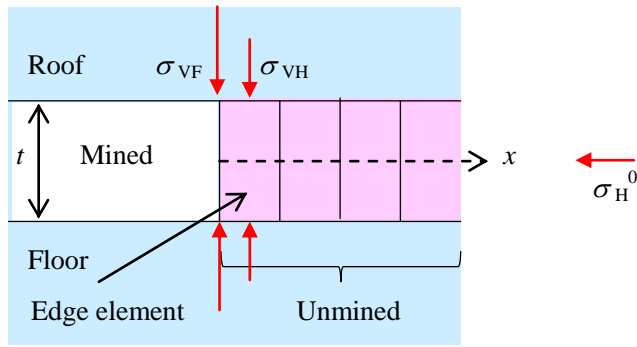
Fig. 5.3 Definition of the variables.

5.3. Results

An attempt to evaluate creep damage of non-edge elements was made. For example, creep damage was calculated for a mining layout (Fig. 5.4a). Normal stress concentration is seen in the vicinity of sidewalls (Fig. 5.4b). Horizontal stress was calculated for $x \leq t$ (Fig. 5.4c). Stress severity was calculated for $x \leq t$ assuming UCS of 80 MPa and internal friction angle of 30° (Fig. 5.4d). Creep damage was calculated assuming $n = 30$ and $\Delta t = 1$ (Fig. 5.4e).
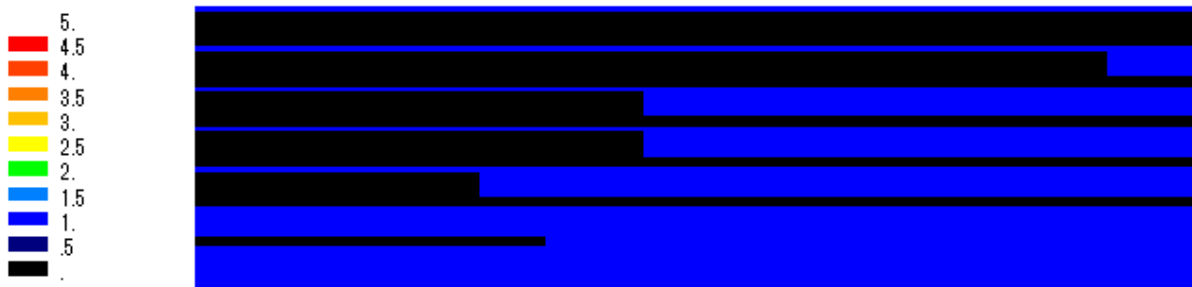
(a) Mining layout (black: mined, blue: unmined).
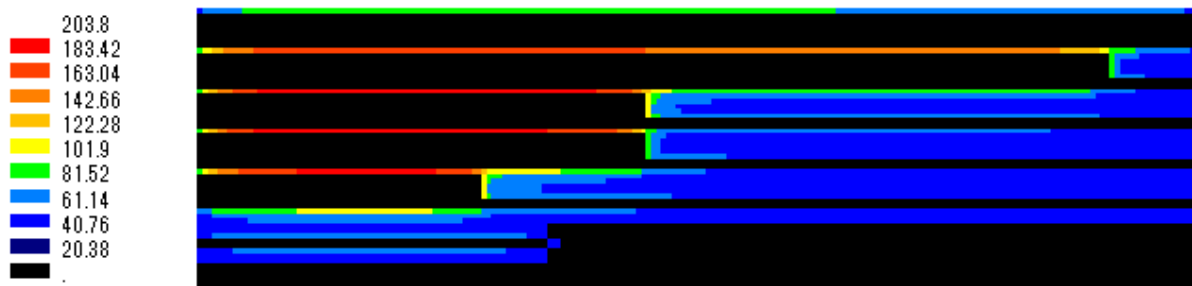
(b) Normal stress (MPa) distribution
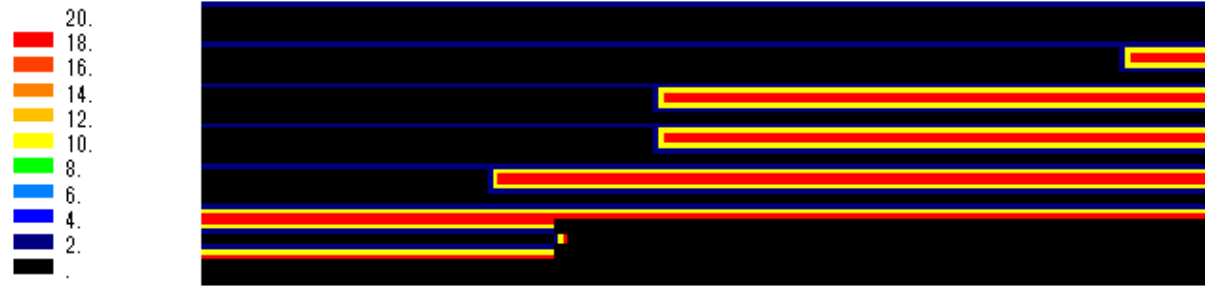
(c) Horizontal stress (MPa) distribution ($x \le t$).
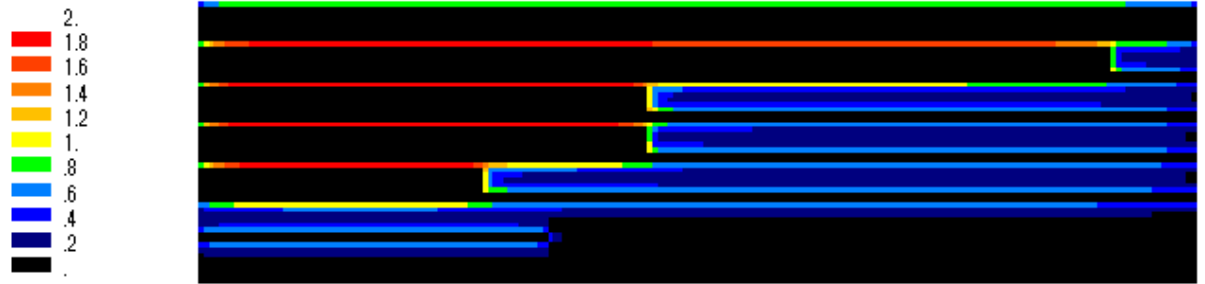
(d) Stress severity ($x \le t$).
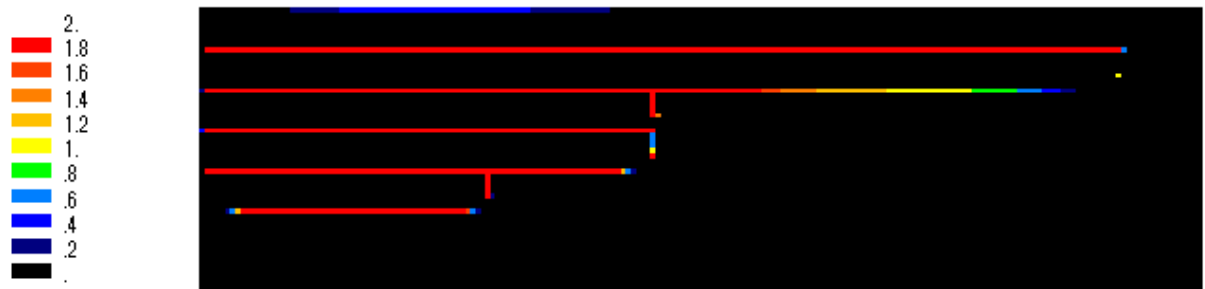
(e) creep damage

Fig. 5.4 Results of creep damage analysis for edge and non-edge elements.

Stress severity is not zero for non-edge elements (Fig. 5.4d). However, creep damage is zero for non-edge elements (Fig. 5.4e). The result suggests that the creep damage analysis can be limited to only edge elements as long as creep damage is calculated based on elastic stress distribution. Therefore, in this study, creep damage for edge elements was evaluated for the rockbursts events.

The cumulative damage for the rockbursts #1, #2, #4, #5, #6, #9, #10 and #12 at the rockburst sites exceeded one (yellow) at rockbursting (after mining) (Fig. 5.5a-j). There are also such areas at the mining faces. However, the rock mass in the vicinity of the mining face is already damaged by blasting and cannot cause violent rockbursts. The number of yellow elements whose damage exceeded one was much more for #12 and this can explain the larger magnitude of #12.

(a) #1 and #2 before mining

(b) #1 and #2 at rockburst

(c) #4, #5 and #6 before mining

(d) #4, #5 and #6 at rockburst

(e) #9 before mining

(f) #9 at rockburst

(g) #10 before mining

(h) #10 at rockburst

(i) #12 before mining

(j) #12 at rockburst
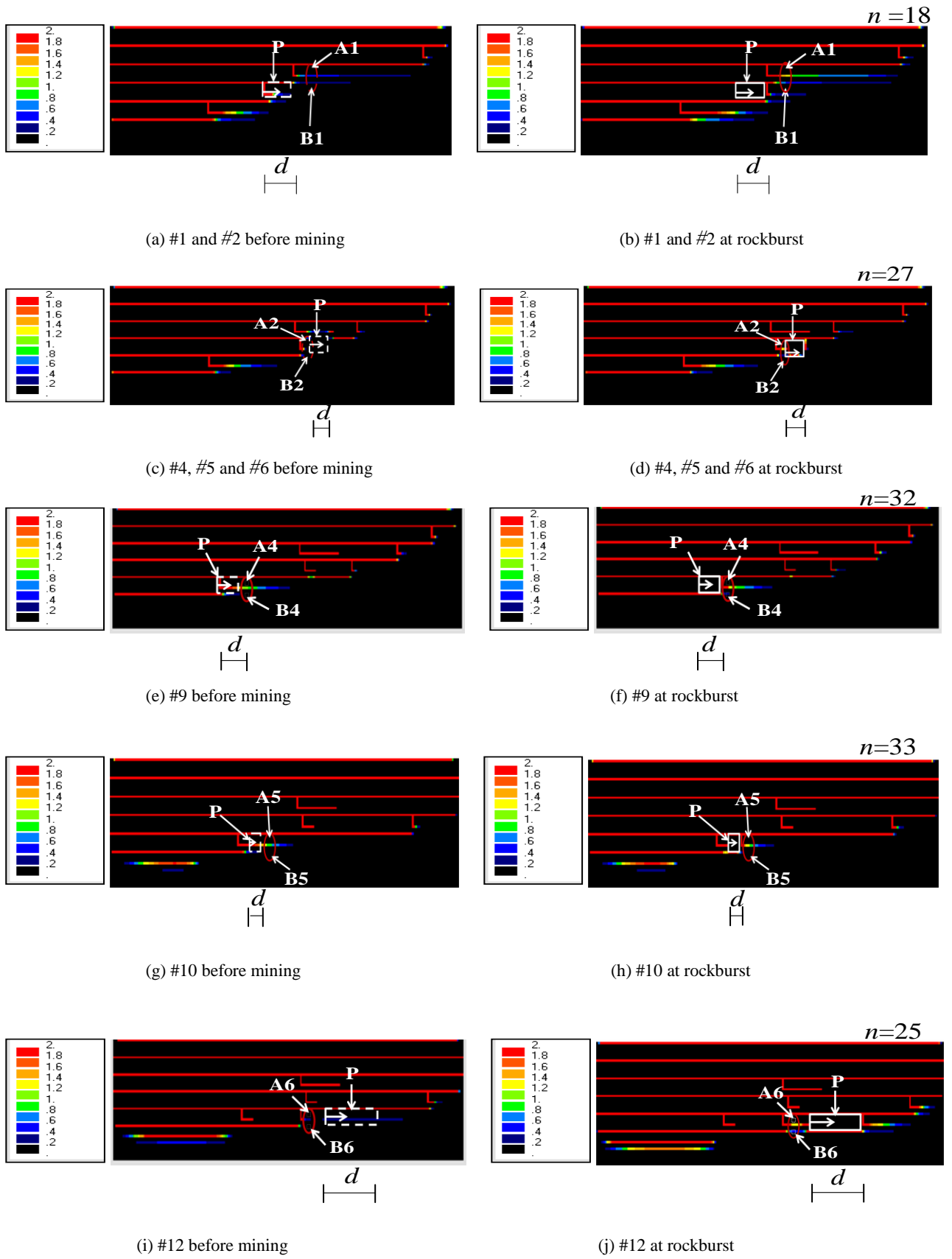
Fig. 5.5 Creep damage evaluation for rockbursts, (all events were well hindcasted except #8, see Fig. 5.9).

(a) #1 and #2 forward direction

(b) #1 and #2 backward direction

(c) #4, #5 and #6 forward direction

(d) #4, #5 and #6 backward direction

(e) #9 forward direction

(f) #9 backward direction

(g) #10 forward direction

(h) #10 backward direction

(i) #12 forward direction

(j) #12 backward direction
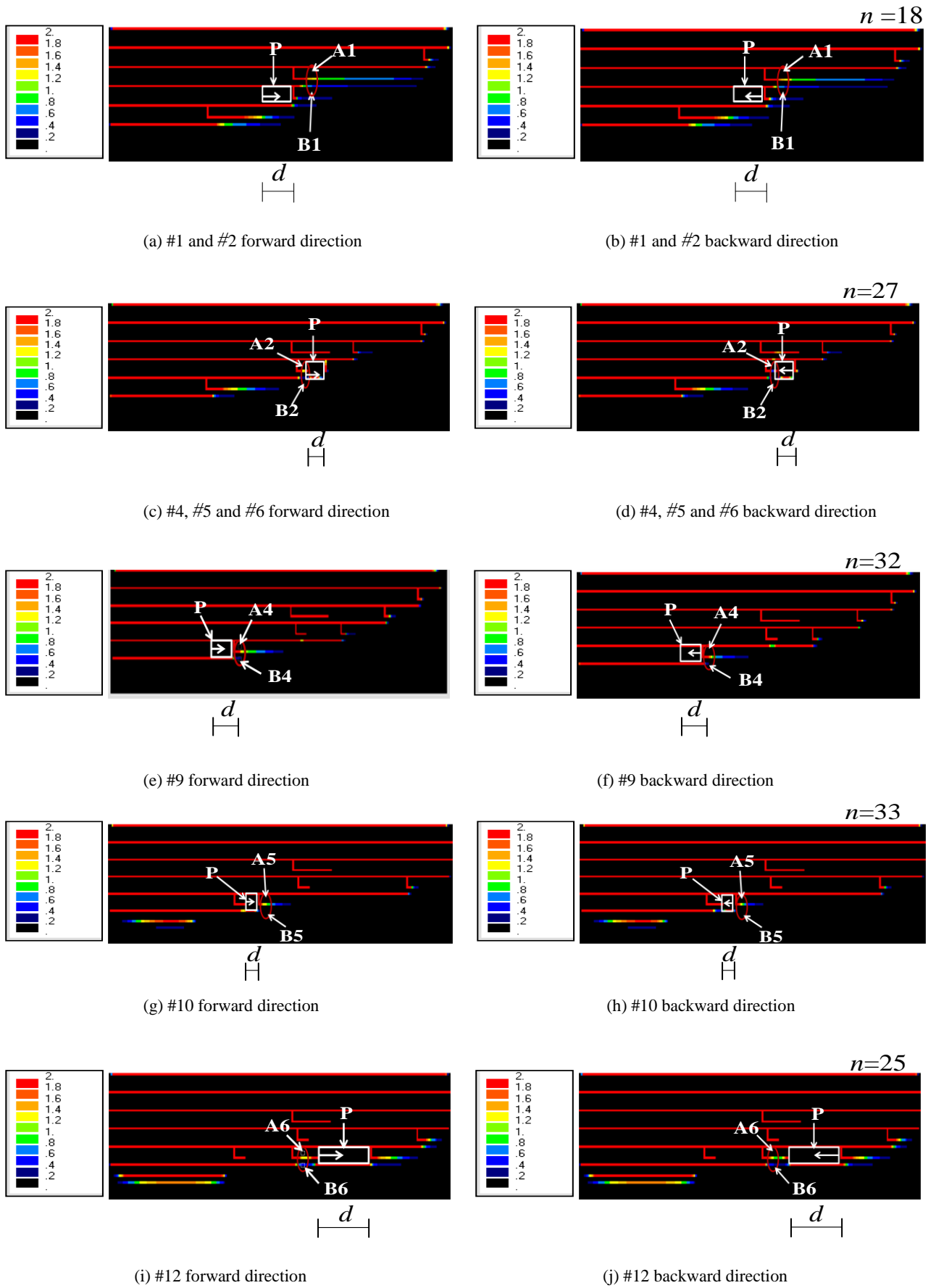
Fig. 5.6 Changing the mining sequence to forward and backward directions, to investigate rockburst potential

The effect of changing the mining sequence on rockbursting potential was investigated (Fig. 5.6). This was achieved by reversing the mining directions, and re-calculating creep damage of the edge elements. Slightly earlier rockbursting was observed after changing the mining sequences for rockbursts #1, #2, #9 and #10. However, rockburst #4, #5, #6 and #12 indicated lower risk of rockbursting after changing the mining sequence.

Creep damage analysis was further carried out to investigate the effect of pillars on rockburst potential (Figs. 5.7 and 5.8). The rockburst cases #4, #5 and #6 (Fig. 5.7f) and #12 (Fig. 5.8f) indicated earlier rockbursting after pillars were eliminated.

Pillars eliminated (illustrated using normal stress distribution figures)   **Creep damage**

(a) The actual case, before eliminating any pillar   (b) #4, #5 and #6 at rockburst

(c) Eliminating top pillar   (d) #4, #5 and #6 at rockburst

(e) Eliminating all pillars near the stope   (f) #4, #5 and #6 at rockburst
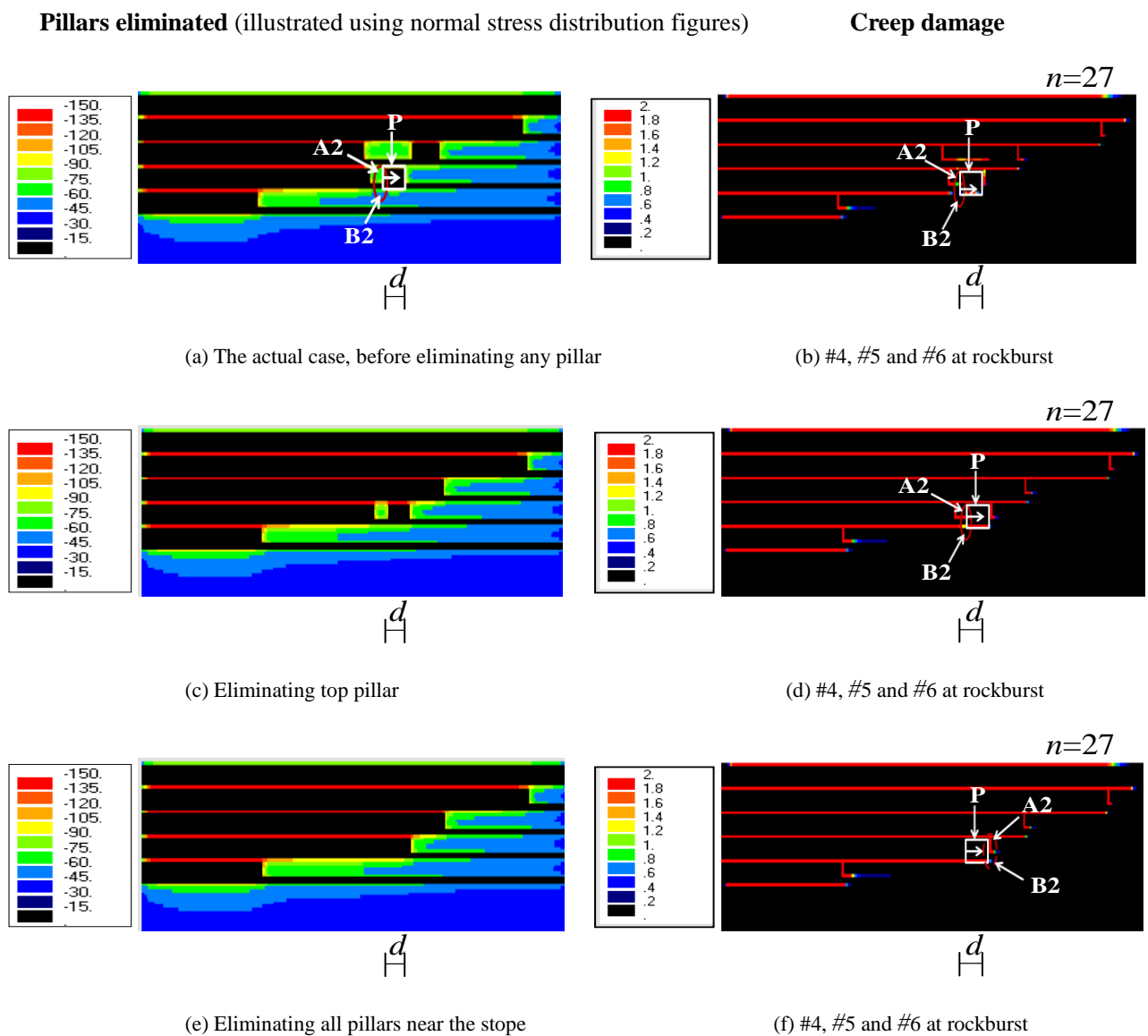
Fig. 5.7 The effect of pillars on rockburst potential for rockbursts #4-6

Pillars eliminated (illustrated using normal stress distribution figures)   **Creep damage**

(a) The actual case, before eliminating any pillar   (b) #12 at rockburst

(c) Eliminating top pillars   (d) #12 at rockburst

(e) Eliminating all pillars near the rockburst site   (f) #12 at rockburst
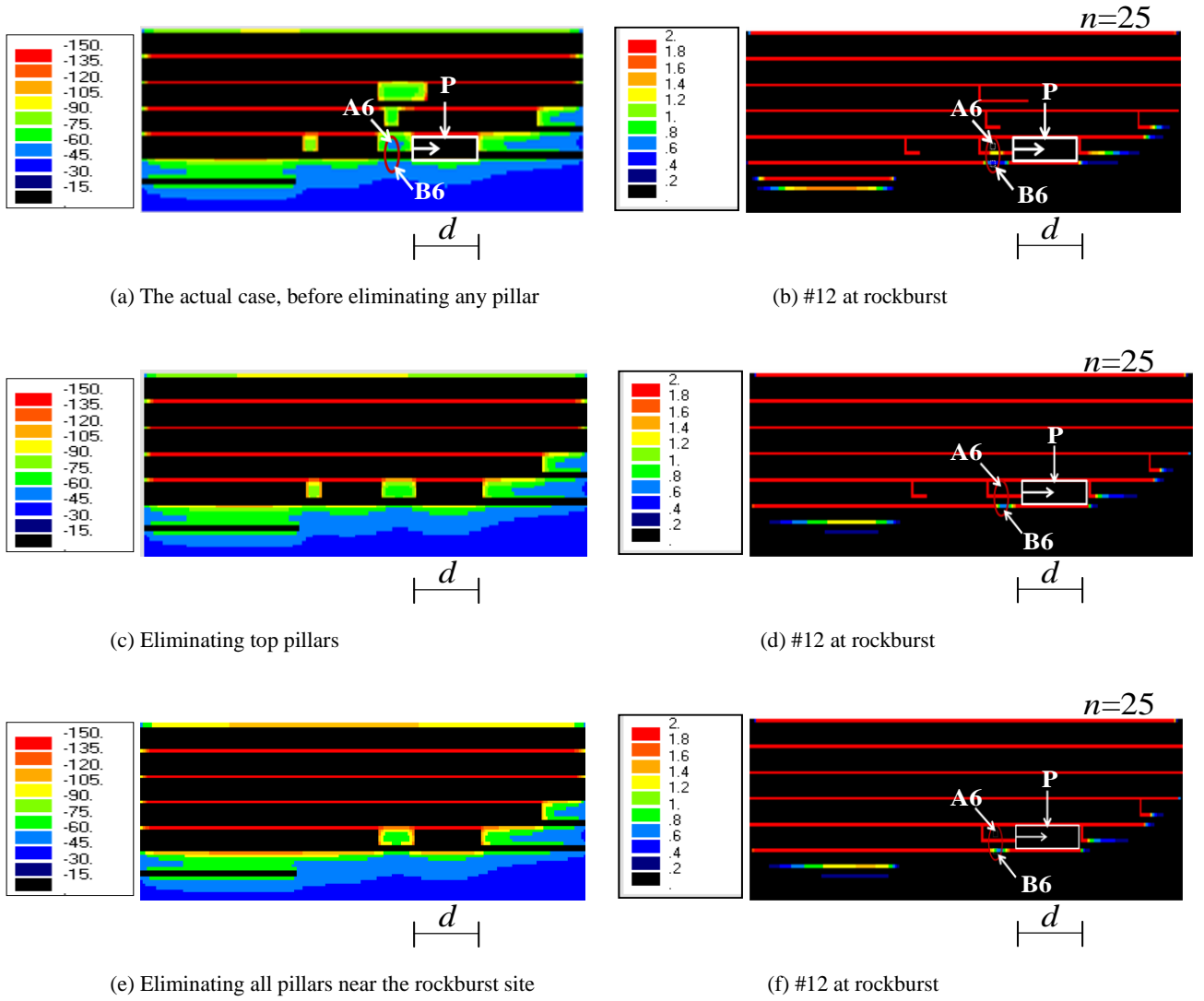
Fig. 5.8 The effect of pillars on rockburst potential for rockburst #12

So far, only rockburst #8 cannot be explained by both by stress increase by mining (Fig 5.9a) and brittle creep failure (Fig. 5.9b). As indicated in Fig. 5.10, it looks like there is moderate to strong correlation between the best values of parameter n (Table 5.1) and distance between rockburst and mining face.
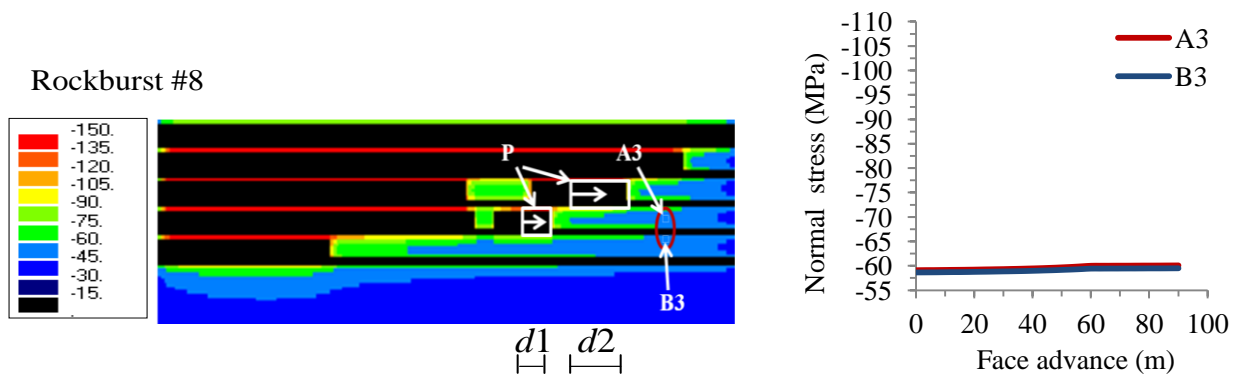
(a) #8 cannot be explained by stress increase by mining
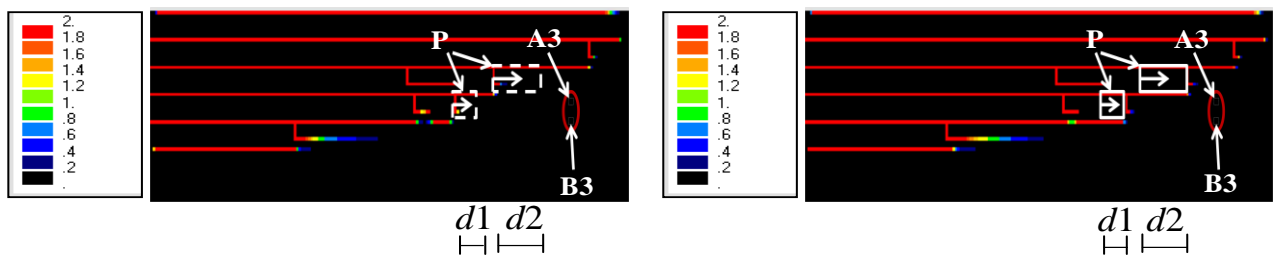
(b) #8 cannot be explained by brittle creep failure

Fig. 5.9 So far rockburst mechanism for #8 cannot be explained
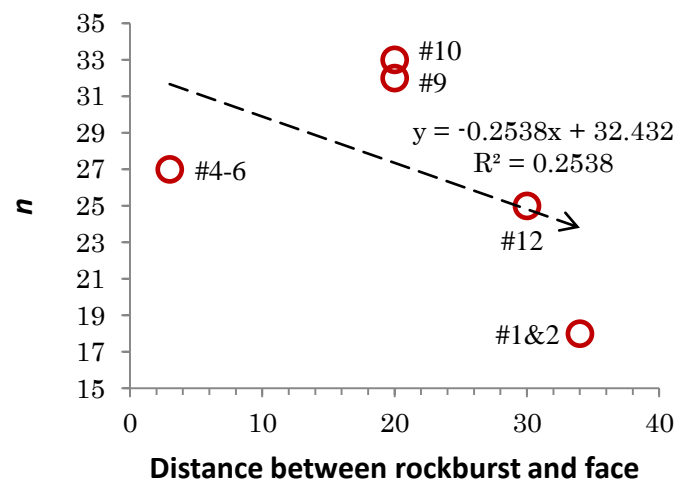
Fig. 5.10 Moderate to strong correlation between the best *n* values and distance between rockburst and face.

6. Elasto-plastic analysis

Various contributions from other researchers have shown that rockbursts in brittle competent rock are common (ex. Jaeger and Cook, 1979; Mazaira and Konicek, 2015; Meng et al., 2021). The rock samples from the Mufulira mine were confirmed to be very hard and brittle (Tables 3.1-3.6), satisfying one of the necessary rockburst occurrence conditions. Another condition is high stress. However, rockbursts did not occur in the chain pillars nor the mining face at which a very high-stress increase was calculated by DDM (Fig. 4.3). The absence of the rockburst occurrences would be due to sequential fracturing of the rock mass by blasting for developing the mining drives and extracting the stopes, as demonstrated by the wide EDZ at 1423 mL (Fig. 2.12b). However, the rockburst occurred in mining drives in diminishing pillars (#4, #5, #6, and #12) or ahead of the face (for #1, #2, #8, #9, and #10) (Fig. 4.3). The rock mass could be relatively intact at the rockburst sites because only blasting for developing the mining drives had been done, as indicated by the small EDZ at 1457 m level (Fig. 2.12a). A gradual increase in stress at the relatively intact rock mass (Fig. 4.5) was expected to satisfy the condition for rockbursts #4-6 and #9 due to the face advance. However, the stress increase for #1, #2, #8, #10, and #12 is minimal (Fig. 4.5a, c, e, and f).

Therefore, a more precise stress analysis was carried out by 2-D FEM considering the 3-D DDM results, which represent the mine-wide mining effects. However, the modified stress severity did not show any significant increase with face advance even for rockburst #9, hence nullifying the possibility of the above rockburst mechanism. Taking the above results into account, a creep damage model as another model for the mechanism of the rockbursts was proposed. The rockbursts were well hindcasted by the model, except for #8 (Fig. 5.9). Different input parameters of *n* (Table 5.1) were used for each rockburst. Fig. 5.10 showed a moderate to strong correlation between *n* and the distance between rockburst and the face. The difference in *n* parameters is a reflection of differences in time-dependent formation in the rock mass for each case of distance between a rockburst and the face. Other influencing factors for the differences could be geometry of the surrounding rock mass.

Damage was also examined for the modified mining sequence to investigate potential of rockbursting. #4-6 and #12 (Fig. 5.6) showed decrease of potential rockbursting after changing the mining sequence. This implies that the risk of rockbursting could be minimized simply by reversing mining directions for those rockburst cases. The effect of pillars on rockbursting potential was also investigated (Figs. 5.7 and 5.8), and both cases indicated earlier rockbursting after pillar removal. Removing some pillars may increase rockbursting risk at the pillars left. However, removing all pillars if possible may decrease rockbursting risks, since no rockburst would be expected at pillars. Rockburst would also not be expected at a stope face, assuming the face has already been fractured.

The damage at the chain pillars indicates far beyond one. Rockbursts there cannot be detected because most

of them are in the mined-out area. The rock mass at the face experiences high-stress concentration, as mentioned above. The area of high-stress concentration is rather narrow and shifts its position with the face advance (Fig. 5.1). The high-stress concentration may induce rock mass failure. However, the rock mass failure is not likely to emerge as severe rockbursts because the area would be narrow, and the rock mass was sequentially already fractured by blasting for extraction.

The creep damage model considers the creep damage; however, DDM is an elastic analysis, and only damage of the edge elements was considered. More precisely, viscous deformation and stress redistribution should be calculated with the effects of the initial stress state. The geological disturbances should also be considered. For instance, rockburst #8 (Fig. 5.9) could not be explained either as instantaneous rock mass failure due to stress increase or brittle creep failure. #8 could possibly be influence by geological conditions such as failure along fault plane or dyke. Similarly, there should be some geological weakness within the region of #1, #2, #4, #5, #6, #10 and #12, although no apparent faults or dykes were found. the pillar behind stope P for #10, and the three pillars in the rockburst area for #1, #2, #4, #5, #6, and #12 (Fig. 4.3) were left during mining because the rock mass was highly fractured. Rockbursts #4, #5, #6 (Fig. 4.3b) and #12 (Fig. 4.3f) occurred after the pillars were formed.

In order to obtain more accurate predictions of rockburst, elasto-plastic analysis is carried out in this chapter.

6.1 Method

Elasto-plastic analysis requires the in-plane stress component, which is normal to the face. The boundary condition is changed to stress-type when the normal and in-plane stresses of an unmined element satisfy the Coulomb criterion, and normal stress is set to $(1 + \sin\phi')/(1 - \sin\phi')$ times the in-plane stress (Fig. 6.1). Namely, no residual cohesion and no change in in-plane stress are assumed. The latter assumption is not precise and should be further investigated in the future.
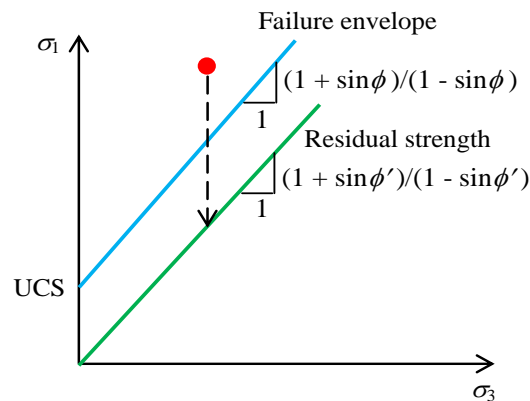
Fig. 6.1 Assumptions in the stress state after satisfying Coulomb failure criterion; $\phi = \phi'$ where ϕ is the internal friction angle and ϕ' is the friction angle on rapture plane.

However, DDM cannot precisely evaluate the in-plane stress. Therefore, in-plane stress obtained by FEM (Fujii and Ishijima, 1994) was approximated by the following equation and used (Fig. 6.2).

$$\sigma_H = \sigma_{H0}(1 - 10^{-0.409\,x/t}) \tag{6.1}$$

where σ_H is the in-plane stress and σ_{H0} is the initial in-plane stress normal to the face, x is the distance from the face, and t is the working height.
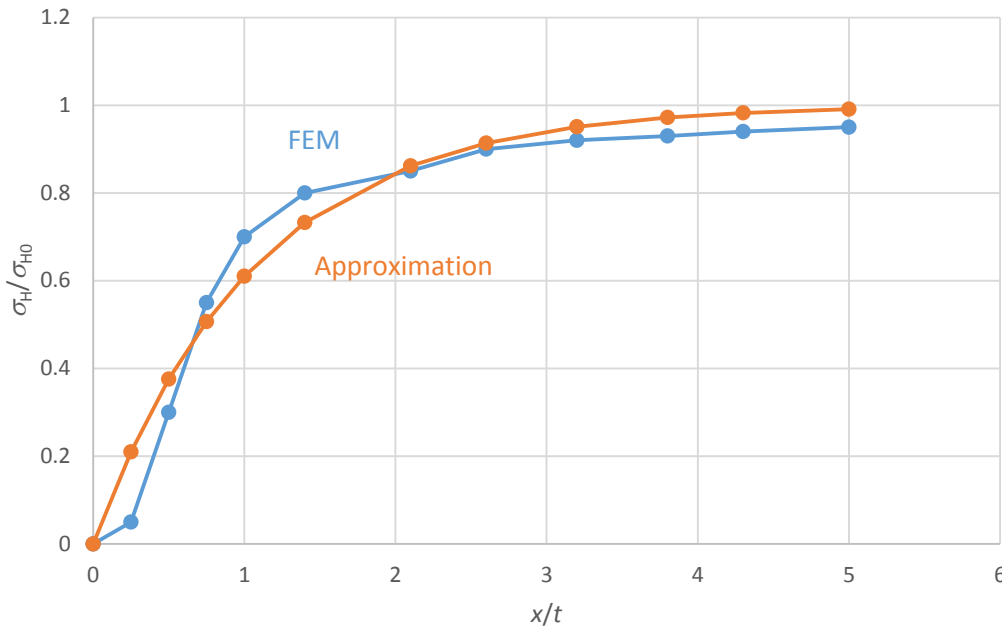
Fig. 6.2 In-plane stress distribution

6.2 Results

The same mining layout and similar input parameters as in the elastic analysis by DDM (Table 4.1) were used. The internal friction angle, ϕ was set to 30° and the UCS range within 130 to 140 MPa was considered. The chain pillars and the outside edges of mining pillars, mining faces, and the sidewalls of the mining drives failed, and the stress concentration on those, including the highest one on the chain pillars, disappeared (Figs. 6.3 and 6.4). Instead, high-stress concentrations can be observed at the mining pillars, faces, and the sidewalls of the mining drives at some distance from the rock surfaces.

At 130 MPa (Fig. 6.4a and b). all the elements near the rockburst site were fractured, indicating that the rock was too weak. Similarly, the UCS values below 138 MPa indicated that the rock was too weak (Fig. 6.4c and

d). However, at UCS 139 MPa the rock was too strong (Fig. 6.4e and f). Therefore, the possibility of rockbursting lies between 138 MPa and 139 MPa, but adjusting UCS values within that small range is not practical. A large scale rockburst was predicted at 140 MPa in the reverse mining direction (Fig. 6.4h). In the actual case, #12 occurred at a pillar in the forward mining direction instead.

It may be worth mentioning that so far the elasto-plastic analysis has not successfully predicted the rockburst events. Therefore more considerations should be made to improve this analysis in future.

UCS =130 MPa

(a) #12 forward direction

(b) #12 backward direction

UCS =138 MPa

(c) #12 forward direction

(d) #12 backward direction

UCS =139 MPa

(e) #12 forward direction

(f) #12 backward direction

UCS =140 MPa

(g) #12 forward direction

(h) #12 backward direction
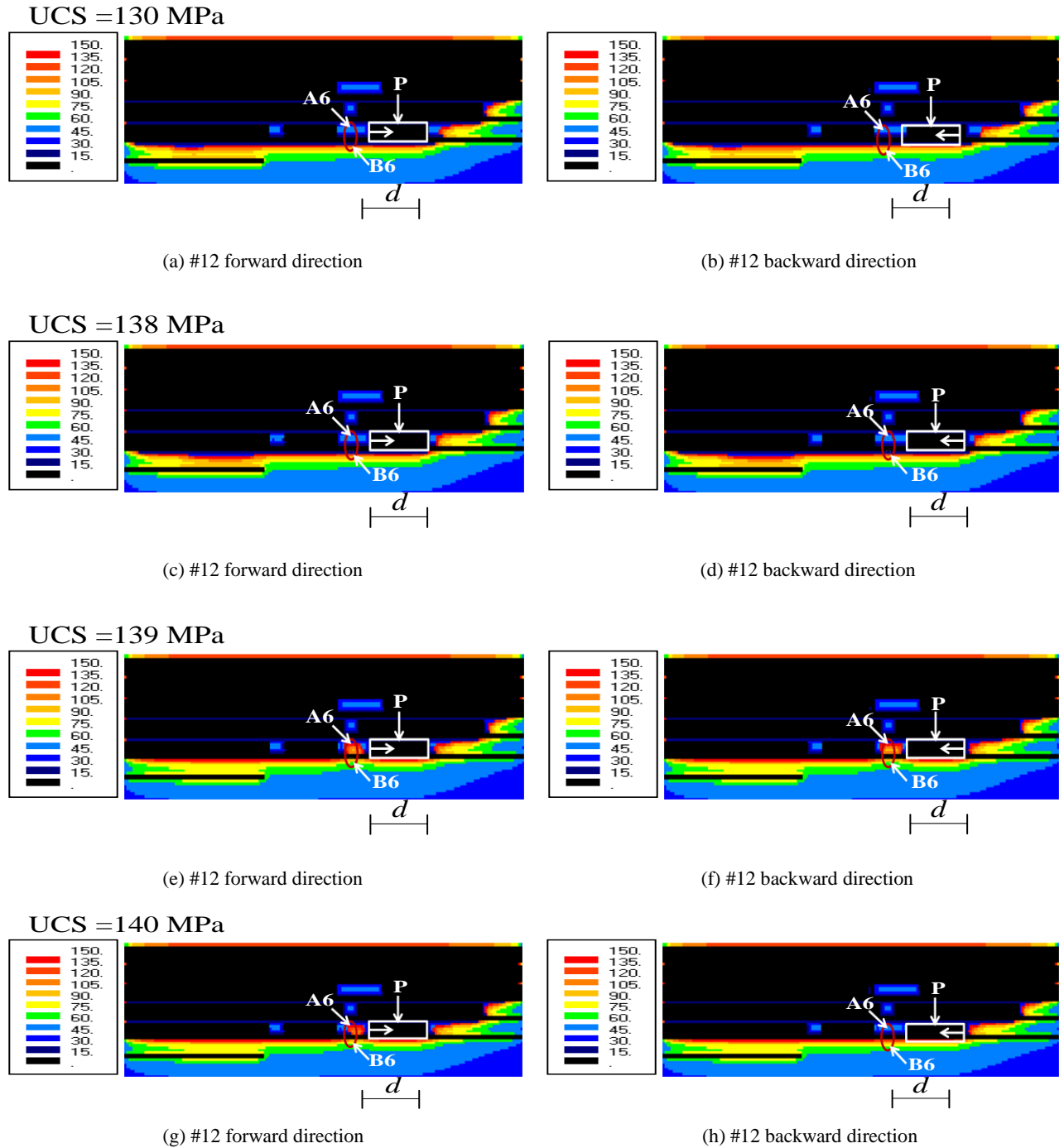
Fig. 6.3 Normal stress distribution

UCS =130 MPa
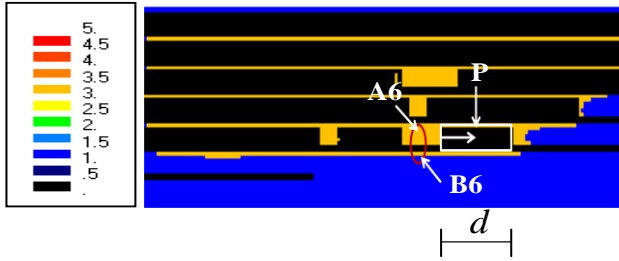
(a) #12 forward direction
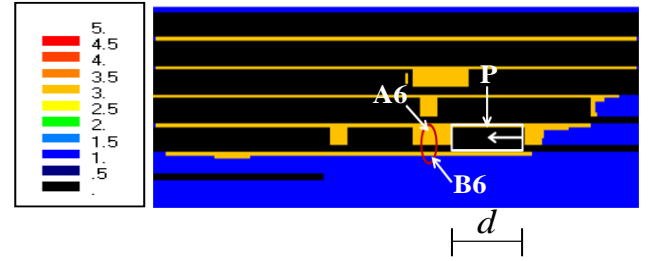
(b) #12 backward direction

UCS =138 MPa

(c) #12 forward direction
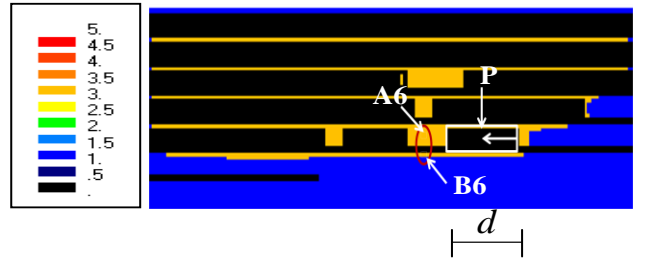
(d) #12 backward direction

UCS =139 MPa
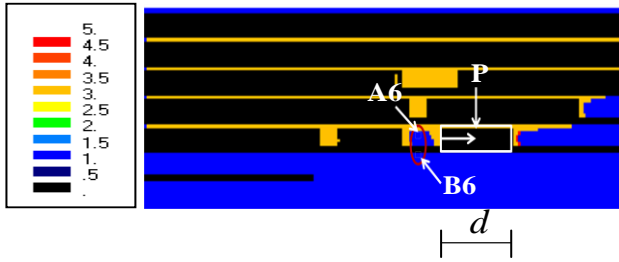
(e) #12 forward direction
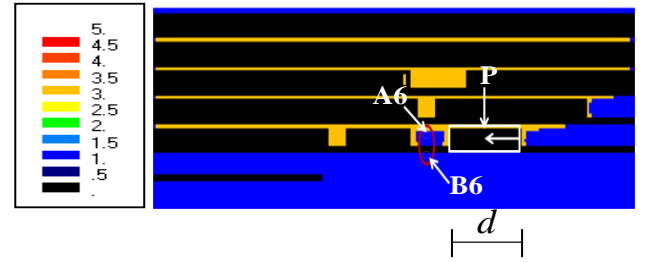
(f) #12 backward direction
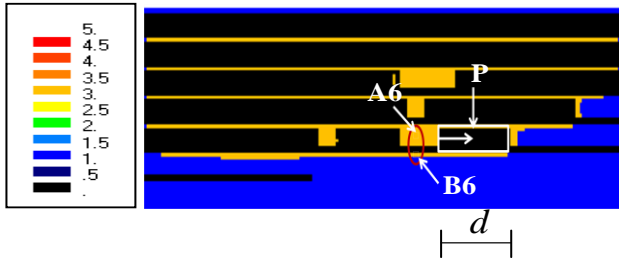
UCS =140 MPa
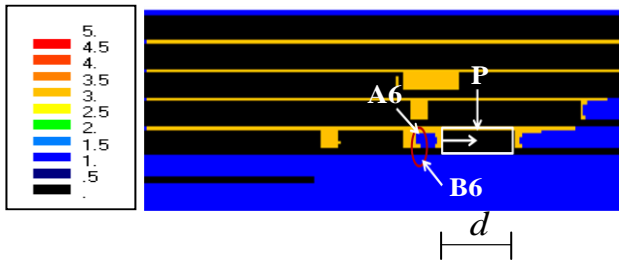
(g) #12 forward direction
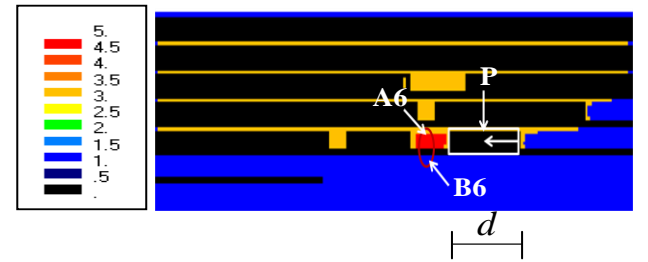
(h) #12 backward direction

Fig. 6.4 Distribution of element failure. Black: mined, blue: unfractured, orange: fractured in the previous steps, red: fractured in this mining step.

7. Source volume of rockburst

Finally, let us consider the source volume of the rockbursts. The widely-used relationship between the seismic moment M0 (N·m) and the moment magnitude M_W is given as

$$\log|M_0| = 9.05 + 1.5M_W \tag{7.1}$$

(Kanamori, 1978; Hanks and Kanamori, 1979). The seismic moment can be represented by the tangent modulus E, Poisson's ratio ν, and the volume change of the source ΔV for a spherical volume source (Fig. 7.1) as

$$M_0 = \frac{(1-v)E}{(1+v)(1-2v)}\Delta V \tag{7.2}$$

(Kumagai et al., 2014). The volume change can be written by the radial displacement ur at $r = r_2$ as

$$\Delta V = 4\pi r_2^2 u_r \tag{7.3}$$

u_r can be calculated from tangential strain ε_θ at r_2 as

$$u_r = -r_2\varepsilon_\theta \tag{7.4}$$

Surrounding rock mass, E, v
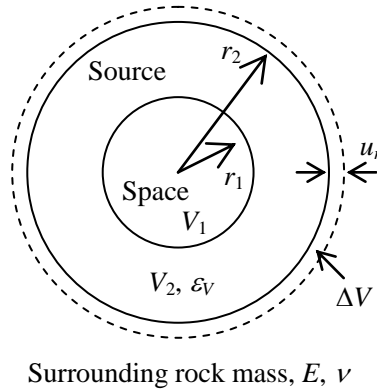
Fig. 7.1Concept of a spherical seismic source with inner space.

where a contraction strain is taken as positive. Let us assume that the space V_1 ($0 \le r \le r_1$) is entirely closed by the fracturing of the source rock mass $r_1 \le r \le r_2$ having the volume V_2,

$$V_1 = -V_2\varepsilon_V - \Delta V \tag{7.5}$$

where ε_V is the volumetric strain of V_2. Then,

$$\frac{4\pi r_1^3}{3} = -\frac{4\pi r_2^3}{3}\varepsilon_V + 4\pi r_2^2 r_2\varepsilon_\theta$$

$$\therefore r_2 = \frac{r_1}{(3\varepsilon_\theta - \varepsilon_V)^{1/3}} \tag{7.6}$$

68

From Eqs. (18), (19), (20), and (22),

$$M_0 = -\frac{3(1-v)}{(1+v)(1-2v)} E \frac{\varepsilon_\theta}{3\varepsilon_\theta - \varepsilon_V} V_1$$

(7.7)

or

$$V_1 = -\frac{(1+v)(1-2v)}{3(1-v)E} \frac{(3\varepsilon_\theta - \varepsilon_V)}{\varepsilon_\theta} M_0$$

(7.8)

For example, substituting $M2.8$ of event #12 into Eq. (7.1), M_0 is calculated as -19.95 TN·m. Substituting this value with Poisson's ratio of 0.222 and $E_{50}r$ of 52.5 GPa for the footwall quartzite into Eq. (7.8),

$$V_1 = \frac{3\varepsilon_\theta - \varepsilon_V}{\varepsilon_\theta} \frac{19.95 \times 10^{12} (\text{N} \cdot \text{m})}{180.3 \times 10^9 (\text{Pa})} = 110.6 \frac{3\varepsilon_\theta - \varepsilon_V}{\varepsilon_\theta} (\text{m}^3)$$

(7.9)

Assuming, for example, ε_θ of 0.02 and ε_V of -0.04, V_1 equals 553 m^3. The geometry of the source is different from the assumed spherical one. However, the unclarified closure length of the mining drive may roughly be estimated by dividing the volume by the sectional area of 16 m^2 as 34.6 m. r_2/r_1 can be estimated by Eq. (7.6) as 2.15 assuming the same strain values. It can roughly be stated that the fractured rock mass thickness would be around 2.3 m, which is 1.15 times the half-width of the mining drive of 2 m. The inward displacement at r_2 can also roughly be estimated by substituting a tangential strain of 0.1 and r_2 of 2.3 m into Eq. (7.4) as 0.46 m. The above estimations are rough and may contain large errors due to unclear assumptions about closure conditions and strain values at rockbursting. However, the estimated values seem almost reasonable, and it is hoped that quantitative descriptions of rockbursts will become possible by a similar but sophisticated method in the future.

7. Concluding remarks

Laboratory tests and numerical analysis were carried out to understand the mechanism of rockbursts at the Mufulira mine. Rockburst did not occur in the chain pillars or at the mining face, but mainly in the mining drives along diminishing pillars or ahead of the mining face. RQD suggested that the rock mass in the rockburst areas was relatively intact (Fig. 2.12a). Laboratory tests confirmed that the rock at Mufulira mine is very strong and brittle (Tables 3.1-3.6). Mine-wide elastic stress analyses for the rockburst sites by 3-D Displacement Discontinuity Method (DDM) indicated very high stress in the chain pillars and low-stress concentration at the sites of rockburst at the initial mining stage (Fig. 4.5), but later, the stress levels gradually increased with progress in mining (Fig. 4.7). However, there was no apparent positive correlation between the elastically calculated stress values and the occurrences of rockbursts (Figs. 4.7 and 4.8). The 2-D elastic FEM analysis was carried out, representing the stress concentration inferred by DDM, and indicated some stress increase with face advance for the rockburst in the vicinity of the mining face. However, stress severity indicated almost no increase (Figs. 4.11 and 4.12), implying that the rockbursts cannot be explained as an instantaneous rock mass failure due to stress increase by mining. Therefore, a creep damage model was newly developed. Cumulative rock damage was evaluated for the edge elements of each sidewall of the mining drives, based on the normal stresses by 3-D DDM. Rockburst occurrences were well hindcasted. Changing the mining sequence may reduce potential rockbursting for some rockburst cases. Ideally, it is best not to leave pillars. However, enough pillars should be used if they are inevitable. Elasto-plastic analysis could not predict the M2.8 successfully. A method to estimate the volume of the rockburst source was proposed, and a likely result was obtained.

In future, experiments will be carried out to confirm creep failure of the quartzite rocks. The effect of discontinuities, such as faults or dykes will be investigated. An investigation will also be carried out to understand the effect of initial rock stress on DDM results. Finally, creep analysis will be combined with elasto-plastic analysis in order to obtain more accurate prediction of rockbursts.

References

Askaripour M, Saeidi A, Rouleau A, Mercier-Langevin P (2022) Rockburst in underground excavations: A review of mechanism, classification, and prediction methods. Underground Space 7 (2022) 577-607.

Aubertin M, Gill DE, Simon R (1994) On the use of the brittleness index modified (BIM) to estimate the post-peak behavior of rocks. Rock mechanics; Models and Measurements; Challenges from Industry. 1st North American Rock Mechanics Symposium, Austin, Texas.

Barton N, Lien R, Lunde J (1974) Engineering classification of rock masses for the design of tunnel support. Rock Mech. Rock Eng., 6(4) (1974), pp. 189-236.

Ben-Guo H, Ravit Z, Yossef HH, Xia-Ting F (2016) Rockburst Generation in Discontinuous Rock Masses. Rock Mech Rock Eng 49(10):4103-4124.

Caw JM (1956) The Kolar Gold Field; Mine and Quarry Engineering. Vol. 22; July, pp. 258-268; August, pp. 306-316. Tothill Press (London).

Crouch SL, Fairhurst C (1973) The Mechanics of Coal Mine Bumps and the Interaction between Coal Pillars, Mine Roof and Floor, U.S.B.M. Contract report, H0101778.

Crouch SL (1976) Analysis of stress and displacements around underground excavations: an application of the displacement discontinuity method. Tech. Rep., Department of Civil and Mineral Engineering, University of Minnesota.

Fairhurst C (1988) Design of Excavations in High Rock-Stress Conditions. Rockbursts and Seismicity in Mines (Proceedings of the 2nd International Symposium, Minneapolis, June 1988), pp. 421-423. C. Fairhurst, Ed. Rotterdam: Balkema, 1990

Fei L, Tianhui M, Chun'an T, Feng C (2018) Prediction of rockburst in tunnels at the Jinping II hydropower station using microseismic monitoring technique. Journal of Tunnelling and Underground Space Technology. 81:480–493.

Fujii Y, Balusu R, Deguchi G, Ishijima Y (2001) Numerical Simulation on Microseismicity due to Mining at One of the Collieries in Australia. 20th Int. Conference on Ground Control in Mining; 9 Aug 2001.

Fujii Y, Kiyama T, Ishijima Y, Kodama J (1999) Circumferential strain behavior during creep tests of brittle rocks. International Journal of Rock Mechanics and Mining Sciences, 36, 323-337.

Fujii Y, Ishijima Y (1994 in Japanese) Approximate Equations to Conveniently Evaluate Stress States in the Vicinity of Longwall Coal Face, Shigen-to-Sozai, Vol. 110, pp. 527-532.

Fujii Y, Ishijima Y, Deguchi G (1997) Prediction of Coal Face Rockbursts and Microseismicity in Deep Longwall

Coal Mining. Int J Rock Mech Min Sci 34(1):85-96.

Goodman RE, (1980) Introduction to Rock Mechanics, John Wiley & Sons, New York.

Hanks TC, Kanamori H (1979) A moment magnitude scale, Journal of Geophysical Research, 84, 5, 2348 - 2350, 9B0059, doi:10.1029/JB084iB05p02348.

He M, Cheng T, Qiao Y, Li H (2022) A review of rockburst: Experiments, theories, and simulations. Journal of Rock Mechanics and Geotechnical Engineering. https://doi.org/10.1016/j.jrmge.2022.07.014

He M, Ren F, Liu D (2018) Rockburst mechanism research and its control. Int J Min Sci Technol 28(5):829-837.

He M, Xia H, Jia X, Gong W, Zhao F, Liang K (2012) Studies on classification, criteria and control of rockbursts. J Rock Mech Geotech Eng 4(2): 97–114.

He S, Lai J, Zhong Y, Wang K, Xu W, Wang L, Liu T, Zhang C (2021) Damage behaviors, prediction methods and prevention methods of rockburst in 13 deep traffic tunnels in China.   Engineering Failure Analysis 121 (2021) 105178.

Hedley DGF (1992) Rockburst handbook for Ontario hardrock mines. CANMET SP92-1E.

Hoek E, Brown ET (1980) Underground Excavations in Rock. The Institute of Mining and Metallurgy, London, p 527.

Jaeger JC, Cook NGW (1979) Fundamentals of Rock Mechanics, 3rd ed., Chapman and Hall, London.

Jing L (2003) A review of techniques advances and outstanding issues in numerical modelling for rock mechanics and rock engineering. Int J Rock Mech Min Sci 40(3): 283-353.

Kaiser PK, Cai M (2012) Design of rock support system under rockburst condition. J Rock Mech Geotech Eng 4 (3): 215–227.

Kaiser PK, Tannant DD, McCreath DR (1996) Canadian rockburst support handbook. Sudbury, Ontario: Geomechanics Research Centre, Laurentian University.

Kanamori H, Stewart GS (1978) Seismological aspects of the Guatemala earthquake of February 4, 1976. Journal of Geophysical Research, 83: doi:10.1029/JB083iB07p03427. issn: 0148-0227.

Kidybin´ ski A (1981) Bursting liability indices of coal. International Journal of Rock Mechanics and Mining Sciences, 18(4), 295–304.

Kumagai H, Maeda Y, Ichihara M, Kame N, Kusakabe T (2014) Seismic moment and volume change of a spherical source. Earth Planets Space 66(7).

Mack MG, Crouch SL (1990) A dynamic boundary element method for modeling rockbursts. In: Proc. 2nd Intl. Symposium on rockbursts and seismicity in mines, Minneapolis. 1988; (ed. Fairhurst C.) (Balkema,

Rotterdam 1990) pp. 93–99.

Malovinchko, D (2020) Description of seismic sources in underground mines: Theory, Bull. Seismic. Soc. Am. 110, 2124-2137, doi:10.1785/0120200093.

Mazaira A, Konicek P (2015) Intense rockburst impacts in deep underground construction and their prevention. Can Geotech J 52(10):1426-1439.

Meng F, Wong LNY, Zhou H (2021) Rock brittleness indices and their applications to different fields of rock engineering: A review. J Rock Mech Geotech Eng 13(1):221-247.

Muller W (1991) Numerical simulation of rock bursts. Int J Min Sci Technol 12(1):27–42.

Neyman B, Szecowka Z, Zuberek Q (1972) Effective methods for fighting rockburst in polish collieries. Proceedings of the 5th international strata control conference, 1–9.

Ng'ambi I, Mutambo V (2016) Optimization of stope recovery and dilution at Mufulira mine through application of appropriate designs and practices. Int J Appl Res 2(9): 397-402.

Ortlepp WD, Stacey TR (1994) Rockburst mechanisms in tunnels and shafts. Tunn. Undergr. Space Technol. 9(1), 59-65.

Perras MA, Diederichs MS (2016) Predicting excavation damage zone depths in brittle rocks. J Rock Mech Geotech Eng 8 (1): 60‑74.

Ryder JA (1988) Excess shear stress in the assessment of geologically hazardous situations. J. S. Afr. Inst. Min. Metall., 88, 27–39.

Russenes BF (1974) Analysis of rock spalling for tunnels in steep valley sides. Department of Geology (247p (in Norwegian).), Norwegian Institute of Technology, Trondheim.

Sainoki A, Mitri HS, Yao M, Chinnasane D (2016) Discontinuum modelling approach for stress analysis at a seismic source: case study. Rock Mech Rock Eng., Vol. 49, No. 12, pp. 4749-4765.

Salamon MDG (1964), Elastic analysis of displacements and stresses induced by mining of seam or reef deposits, Part IV, Inclined reef, J. S. Afr. Inst. Min. Metall., Vol. 65, No. 5, pp. 319-338.

Sepehri M, Apel D.B, Adeeb S, Leveille P, Hall R.A (2020) Evaluation of mining-induced energy and rockburst prediction at a diamond mine in Canada using a full 3D elastoplastic finite element model. Eng. Geol. 266, 105457.

Sheng-Jun M, Mei-Feng C, Qi-Feng G, Zheng-Jun H (2016) Rock burst prediction based on in-situ stress and energy accumulation theory. Int J Rock Mech Min Sci 83:86–94.

Singh SP (1989) Classification of mine workings according to their rockburst proneness. Mining Science and

Technology, 8(3), 253–262.

Sinkala P, Nishihara M, Fujii Y, Fukuda D, Kodama J (2019) Investigation of Rockburst in Deep Underground Mines, A case study of Mufulira mine, Copperbelt, Zambia, Annual Meeting of ARMA (American Rock Mechanics Association). 219;19-16, 23-26 June 2019, NY.

Sinkala P, Nishihara M, Nakayama Y, Fujii Y, Kodama J, Fukuda D, Chanda E (2022) Creep Damage Model for Rockburst at Mufulira Mine in Zambia. Mining, Metallurgy & Exploration. 39. 10.1007/s42461-022-00668-z.

Sirait B, Wattimena RK, Widodo NP (2013) Rockburst prediction of a cut and fill mine by using energy balance and induced stress. Procedia Earth and Planetary Science 6(2013) 426-434.

Tao ZY (1988) Support design of tunnels subjected to rockbursting. Rock Mechanics and Power Plant, ISRM International Symposium, Madrid, Spain.

Tian-Hui M, Chun-An T, Shi-Bin T, Liang K, Qun Y, De-Qing K, Xu Z (2018) Rockburst mechanism and prediction based on microseismic monitoring. Int J Rock Mech Min Sci 110:177–188.

Turchaninov IA, Markov GA (1981) Conditions of changing of extra-hard rock into weak rock under the influence of tectonic stresses of massifs. Proc. Int. Sympos. Weak Rock, Tokyo, 21 (1981), pp. 555-559

Wang JA, Park HD (2001) Comprehensive prediction of rockburst based on analysis of strain energy in rocks. Tunnelling and Underground Space Technology, 16(1), 49–57.

Wang QW, Ju NP, Du LL, Huang J, Hu Y (2018) Three dimensional inverse analysis of geostress field in the Sangri-Jiacha section of Lasa-Linzhi railway. Rock Soil Mech., 39 (4), 1450-1462.

Wang YH, Li WD, Li QG, Xu Y, Tan GH (1998) Method of fuzzy comprehensive evaluations for rockburst prediction. Chinese Journal of Rock Mechanics and Engineering, 17(5), 493–501 (in Chinese).

Yoon JS (1994) Tunnel Engineering, 160-162.

Zhang L, Einstein HH (2004) Using RQD to Estimate the Deformation Modulus of Rock Mass. Int J Rock Mech Min Sci 36(5): 337-342.